National and Kapodistrian University of Athens

Evaluating the impact of the radio jet in the evolution of the galaxies

Athanasia Gkogkou
R.N.: 2018303

Supervisor: Kalliopi Dasyra

Athens, July 2020

Evaluating the impact of radio jets in the evolution of galaxies

by

Athanasia Gkogkou

R.N.: 2018303

Supervisor: Assistant Professor K. Dasyra

Member of committee: Associate Professor N. Vlahakis

Member of committee: Assistant Professor S. Kazantzidis

A thesis submitted in partial fulfillment for the
degree of MSc in Physics

in the
Faculty of Science
Physics Department

July 2020

Abstract

Throughout the last years there were many detections of galactic winds, both in ionized and molecular state, suggesting them an active field in the astronomical community. One of the first questions one needs to answer is what is the mechanism triggering these winds. The two suggested mechanisms are the quasar mode, according to which the AGN's radiation pressure is the driving source, and the radio mode where the radio jet is responsible for the wind. In order to shed light on which one of the two mechanisms is more possible I follow two steps. Firstly I re-evaluate the driving mechanism of a sample of 45 galaxies, already published, and secondly a new sample of radio galaxies selected by our team. In the later case, in order to test whether the radio jet is capable of driving an outflow I perform SED fitting. In this way I estimate the radio jet's power and the binding energy of the galaxy, and by combining this information I obtain a timescale that can show whether the scenario of the radio mode is possible.

Key words: *galactic outflows, radio jets, AGN, SED-fitting, AGN feedback*

Περίληψη

Τα τελευταία χρόνια έχουν παρατηρηθεί πολλοί μαζικοί άνεμοι σε γαλαξίες, είτε σε ιονισμένη είτε σε μοριακή κατάσταση, καθιστώντας τους ένα πολύ σημαντικό θέμα μελέτης στην αστρονομική κοινότητα. Ένα από τα πρώτα ερωτήματα που θέτει κανείς είναι ποιος είναι ο μηχανισμός που πυροδοτεί αυτούς τους ανέμους. Οι δύο πιθανές απαντήσεις, σε περίπτωση που οι άνεμοι σχετίζονται με μαύρη τρύπα κι όχι με αστρογέννεση, είναι η πίεση ακτινοβολίας από τον AGN (quasar mode) και η εναπόθεση ενέργειας από τον ραδιοπίδακα (radio mode), με την πρώτη να χρησιμοποιείται στην βιβλιογραφία ως πιο συχνή εξήγηση. Η επανεξέτασή μας μιας ομάδας 45 γαλαξιών, ήδη δημοσιευμένων, έδειξε ότι το radio mode μπορεί να είναι τελικά πιο πιθανός μηχανισμός. Γι' αυτόν τον λόγο το επόμενο βήμα ήταν η μελέτη μιας καινούριας ομάδας ραδιογαλαξιών, στην οποία θελήσαμε να ερευνήσουμε σε πόσους από αυτούς εντοπίζουμε ανέμους και αν είναι πιθανό ο άνεμος αυτός να προκαλείται από τον ραδιοπίδακα. Επομένως, το πρόβλημα ανάγεται στον υπολογισμό της ισχύος του ραδιοπίδακα και της δυναμικής ενέργειας και μάζας των γαλαξιών. Για το σκοπό αυτό πραγματοποιώ SED fitting, δηλαδή προσέγγιση των παρατηρησιακών δεδομένων του εκάστοτε γαλαξία, από το καταλληλότερο μοντέλο με χρήση Bayesian στατιστικής. Κάθε μοντέλο κατασκευάζεται με τέτοιο τρόπο ώστε να περιγράψει την ακτινοβολία της κάθε συνιστώσας του γαλαξία (αστέρια, σκόνη, AGN, ραδιοπίδακας). Έπειτα υπολογίζω την ισχύ του ραδιοπίδακα, από την πολυχρωματική ροή του, καθώς και την δυναμική ενέργεια του γαλαξία από την μάζα των αστεριών. Δημιούργησα έναν νέο κώδικα, τον οποίο εφάρμοσα σε 3 γαλαξίες (PKS 1005+007, NGC 3100, J1109-3732). Τελικός σκοπός της εργασίας μου είναι να ακολουθηθεί αυτή η διαδικασία και για τους 70 ραδιογαλαξίες που μελετάμε, ώστε να προκύψουν στατιστικά αποτελέσματα.

Λέξεις κλειδιά: *Γαλαξιακοί άνεμοι, Ραδιοπίδακες, Ενεργοί Γαλαξιακοί Πυρήνες, SED-fitting, AGN feedback*

Contents

List of Figures

List of Tables

Abbreviations

ISM   **I**nterstellar **M**edium

AGN   **A**ctive **G**alactic **N**uclei

SED   **S**pectral **E**nergy **D**istribution

SSP   **S**imple **S**tellar **P**opulation

SFH   **S**tar **F**ormation **H**istory

SFR   **S**tar **F**ormation **R**ate

IMF   **I**nitial **M**ass **F**unction

BBB   **B**ig **B**lue **B**ump

PDF   **P**robability **D**ensity **F**unction

BIC   **B**ayesian **I**nformation **C**riterion

MCMC   **M**onte **C**arlo **M**arkov **C**hain

Chapter 1

Introduction

Recently, detections of molecular outflows are systematically being discovered and have occasionally been attributed to radio jets. The regularly-moving gas in galaxies tends to rotate with a velocity defined by angular momentum in a gravitational potential that stars and dark matter form. Galactic winds are identified as gas flows whose velocity exceeds the rotational and dispersion velocity of the corresponding galaxy. Through the last 40 years there have been plenty of observations of galactic winds (Sakamoto et al. 2006, 2009, Leon et al. 2007, Feruglio et al. 2010, Fischer et al. 2010, Alatalo et al. 2011, Rangwala et al. 2011, ?, Krips et al. 2011, Dasyra, Combes 2011, Aalto et al. 2012a, Tsai et al. 2012, Morganti et al. 2013, Combes et al. 2013, Spoon et al. 2013, Veilleux et al. 2013, Cicone et al. 2014, Garcia-Burillo et al. 2014; ?, George et al. 2014, Sakamoto et al. 2014, Alatalo et al. 2013, Tombesi et al. 2015, Aalto et al. 2016, Stone et al. 2016, González-Alfonso et al. 2017, Pereira-Santaella et al. 2018, Fluetsch et al. 2018) making their study a key area of research.

Multiwavelength observations show that galactic winds appear in different phases, which can be generally divided into three categories: ionized (hot or warm, $\sim 104K$), neutral atomic (cool, $\sim 103K$), and molecular (cold $\leq 100K$) (Heckman, Thompson, 2019). Their basic properties, like velocity, mass outfow rate, spatial extent, depend on the type of the galaxy and the phase of the outflow. Their velocities can range from a few hundred km/s to thousand km/s, their mass outflow rates $\sim 10^{-1} - 10^3 \; M_\odot yr^{-1}$ and their extent from a few parsecs up to $\sim 20kpc$.

The source of energy of galactic winds can be either the starburst regions or the active nucleus of the host galaxy. In both cases energy exceeding the binding energy of the gas is deposited to the surrounding ISM creating the outflow.

High luminosity AGNs are close to their Eddington limit so the radiation pressure coming from the central engine can stop the inflow of the accreting material. This leads to the ejection of the surrounding ionized gas creating an initial ionized wind moving with velocity v_{in}. However, neither the radiation pressure that created the ionized outflow nor the ram pressure exerted by it on the molecular gas is enough to explain the more massive molecular outflows that have been observed. So momentum boosting was included to explain the wind.

Starburst winds are driven by the mechanical energy and momentum from stellar winds and supernova explosions. In the case of AGNs the wind is driven either by the AGN's radiation pressure (quasar mode) or the radio jet (radio mode).
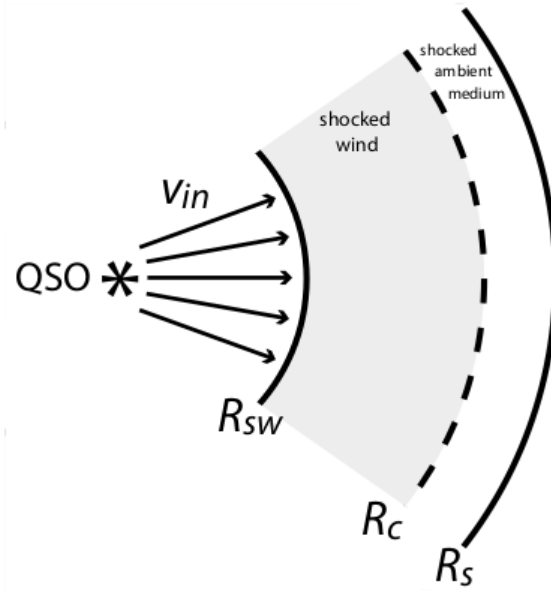
FIGURE 1.1: Scheme of the wind structure. An initial ionized wind is ejected by the AGN, with velocity v_{in}. The ionized wind shocks the ISM at radius R_c, the forward shock front exists at radius R_s and the reverse one at radius R_{sw} (taken from Faucher-Giguere, Quataert, 2012)

The ionized outflow shocks against the ambient material creating two shock fronts, in the same way that studies of fast stellar winds have shown (Weaver et al., 1977). The outer shock propagates towards the ISM and the reverse one towards the initial wind (Fig.1.1). When the ionized medium between the two shocks (between R_{sw} and R_s) is

tenuous enough to not be able to cool in the timescale of the shock front propagation thermal energy is conserved. Part of this energy transforms into kinetic energy leading to an adiabatic expansion and the rest of it transforms into thermal pressure of the shocked material. Now, the thermal pressure exerted on the surrounding molecular gas can create a molecular outflow like those observed, as it performs PdV work.

An alternative mechanism to radiation is radio jets driven by black holes. The same physical procedures happen for the cavity of a relativistic jet propagating through the ISM, which happens to galaxies with low AGN luminosity (Wagner, Bicknell, 2011). The thermal pressure exerted by the expanding cavity on the molecular clouds creates a massive molecular outflow, in the same way mentioned before. However, in this case, the adiabatic expansion happens instantaneously and lasts throughout the whole jet propagation time and with greater efficiency, due to local deposition of energy.

Until recently the quasar mode was the most common explanation of the observed molecular outflows because for most sources there was little or no excess of radio emission compared to the infrared emission of these galaxies. Radio excess is the ratio of infrared luminosity over luminosity at 1.4GHz (q_{ir}) (e.g. Ivison et al., 2010). Typical values of q_{ir} for radio loud galaxies are $q_{ir} < 1.8$, so if the ratio of the galaxy one studied was much higher than 1.8 it was assumed to not host a radio jet hence automatically the explanation of the observed outflow would be the quasar mode. However, this is not a safe criterion and the following examples can prove it.

NGC1377 is a nearby elliptical galaxy (Fig. 1.2) with a small disk in its center, discovered in CO with ALMA. In the dispersion map of the molecular gas a jet-like outflow along the minor axis is revealed (Aalto et al., 2016). Therefore, the jet-shaped wind in this galaxy indicates the passage of a jet from the ISM, even though no radio emission was observed before. So, according to the radio excess criterion radio mode is immediately ruled out. Although, this is untrue since the jet is too faint to be observed via its synchrotron emission.

Another example proving the inadequacy of radio excess as the only criterion used for the understanding of a galactic outflow's driving mechanism is the spiral galaxy ESO420-G13 (Fernández-Ontiveros et al., ????). In the velocity dispersion map (Fig. 1.3 (A)) there is a region of unexpectedly high dispersion along the galaxy minor axis. This is an outflow, which clearly does not follow the rotation velocity of the galaxy: it has higher
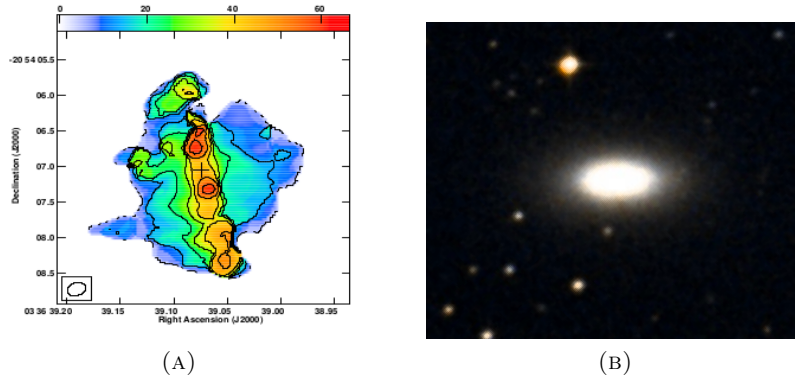
FIGURE 1.2: (A) Velocity map of galaxy NGC1377 (Aalto et al., 2016). A jet-like outflow can be distinguished. (B) Optical image of NGC1377 (HST)

velocities than even the gas along the major axis. Additionally, there is ionized gas linearly connecting the nucleus to the outflowing region: the contours in the center represent the [NeII] emission (Fig. 1.3 (B)). The molecular outflow has a linear component along the same direction with [NeII], at the end of which starts a funnel-shaped structure, which is shown in the velocity range of 130km/s, at the right panel of Fig. 1.3. This is known to happen when a jet propagates through the ISM and then bifurcates when it encounters a dense cloud, as in the case of IC5063 (Morganti et al., 2015; Dasyra et al., 2016). As before, the shape of this outflow is indicative of the existence of a jet. This was previously unknown, as the radio emission in this galaxy was unresolved in galaxy scales.
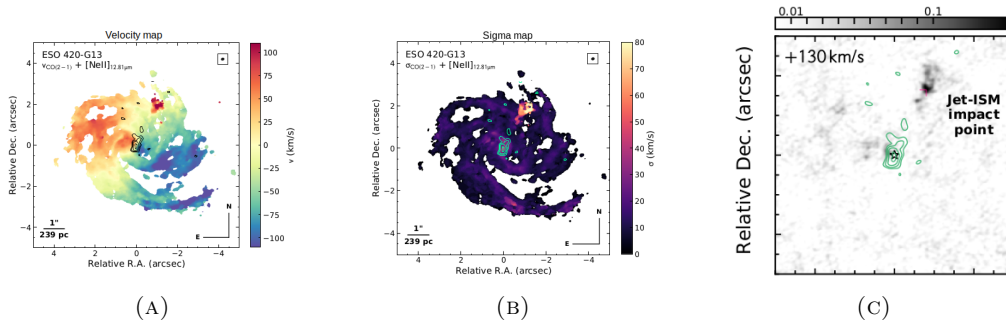
FIGURE 1.3: (A) Velocity map of galaxy ESO420-G13(B) Dispersion map (C) CO(2-1) channel map at $130kms^1$. The green-solid contours correspond to the integrated $[Ne_{II}]$ $12.8\mu m$ emission from VISIR.

Chapter 2

Searching for jet-driven outflows

Having examples like the two galaxies above, it is foreseeable that the radio mode could be an equally possible mechanism as the so far used quasar mode. To test this theory a sample of galaxies with already detected molecular outflows is re examined in the following section.

2.1   Literature-based sample

Starting by the sample presented in Cicone et al. (2014) and expanded by Fluetsch et al. (2018) and some more recent outflow detections in the literature (Runnoe et al., 2017; Audibert et al., 2019; Fernández-Ontiveros et al., ????), I evaluated how many outflows in these galaxies could be jet-driven. I applied several more criteria to that of Fluetsch et al. (2018), who simply considered the radio excess. To determine the upper and lower fraction of jet-driven winds in our sample I defined three categories after having rejected starburst from the Fluetsch et al. (2018) sample.

The first category includes galaxies that have diffuse radio emission associated with a radio jet which drives the detected molecular outflow, as claimed in the studies presenting the detection. One of the most known in the category of galaxies that hold a jet-driven outflow is IC5063 galaxy (Morganti et al. 2015, Dasyra et al. 2016) where the molecular outflows are observed at the regions that the jet interacts with the ISM. Another very well known case is, the above mentioned, LINER galaxy NGC 1377 where there has been detected a jet-like molecular outflow that led us to the conclusion that there is a faint radio

jet (Aalto et al. 2012b). In Seyfert 2 galaxy NGC 1068 there is a collimated molecular outflow in the central region, along the NE-SW direction (**?**). As one can obtain from the radio emission map of this galaxy there is a small radio jet along the same direction that spatially coincides with the molecular outflow (Garcia-Burillo et al. 2014). NGC 3256 is a merging system and although it is classified as a HII galaxy the southern nucleus presents strong evidence for a jet-driven outflow (Sakamoto et al. 2014). Another case is the Seyfert 2 galaxy, M51, where the molecular outflows are detected at regions that outline the radio jet. An apparent relation between the radio jet and the molecular outflow was done by Querejeta et al. (2016). Except for the galaxies in Fluetsch et al. (2018) sample we include two extra galaxies that fall into this category. NGC 613 is a Seyfert type galaxy with a radio jet detected at its central area and a molecular outflow originating from the same spot. The only possible driving mechanism, as indicated by the authors (Audibert et al. 2019), is the radio jet. Additionally, Seyfert 2 galaxy ESO 420-613 is a similar case to NGC 1377 where the detected collimated molecular outflow revealed the existence of a radio jet which is responsible for the outflowing gas (Fernández-Ontiveros et al. ????).

The second category has to do with galaxies hosting jet-driven ionized outflows so there is also molecular content in the wind. 4C 12.50, which falls into this category, is a Seyfert 2 galaxy with a circumnuclear molecular outflow at the same region where there is radio emission from a jet. It is also important that an outflow of atomic gas has been observed at the nucleus of the galaxy (Fotopoulou et al., 2019). In Mrk 1014 there is an ionized outflow that is tightly associated with the radio jet (Husemann et al. 2013) and a molecular outflow (Fluetsch et al. 2018) that seems to be along the same direction as the jet. Also in NGC 5643 galaxy an ionized outflow has been detected which coincides with the radio jet's axis (Cresci et al. 2015). There are indications for a molecular outflow (Alonso-Herrero et al. 2018, Fluetsch et al. 2018 presents an upper limit for the outflow's mass rate) which could be the result of the interaction between the ionized outflow and the radio jet . Finally, NGC 1386 appears to have an ionized outflow supported by the galaxy's radio jet (Rodríguez-Ardila et al. 2017) while the distribution of the molecular gas seems to be along the jet's axis (Mezcua et al. 2015). NGC 1266, a LINER galaxy, according to Alatalo et al. (2011) has an AGN-driven molecular outflow perpendicular to the stellar disk of the galaxy. Along this direction there is an extended radio emission most likely coming from a radio jet. Davis et al. (2012) has also observed an ionized outflow at the same direction as the extended radio emission, making us confidently assume that

this galaxy holds a jet-driven molecular outflow.

Finally, the third category consists of galaxies with molecular outflows at the same direction and extent as their radio jet. More specifically, in the following galaxies there is a most likely jet-driven ionized outflow so it is highly anticipated that they have a jet-driven molecular outflow as well, since galactic winds appear to be multiphase in general. In the Circinus, which is a Seyfert 2 type galaxy, Zschaechner et al. (2016) has pointed out a molecular outflow at the northwestern region of the nucleus. In this galaxy there is a prominent radio jet perpendicular to the galactic disk (Elmouttie et al. 1995) that can be spatially correlated with the outflow region. Another case is that of NGC 1433 galaxy where a molecular outflow is detected along the galaxy's minor axis (Combes et al. 2013). According to radio observations presented in Harnett (1987) there is extended radio emission along the same direction that the outflow is observed. Mrk 231 is a Seyfert 1 galaxy with unambiguous molecular outflow at the circumnuclear region (Feruglio et al. 2015) where there is also extended radio emission indicating the existence of a radio jet (Taylor et al. 1999). NGC 6764 is a LINER galaxy with the radio emission of the jet perpendicular to the disk. It also has a molecular outflow located to the north of the nucleus coinciding with the jet's axis (Leon et al. 2007). Finally, a mainly nuclear molecular outflow has been detected in Mrk 273 galaxy with an extension to the north of the nucleus (Cicone et al. 2014). **?** have observed radio emission at the very center of Mrk 273 hinting an association between the outflow and the potential radio jet (González-Alfonso et al. 2017).

So, after re-evaluating the Fluetsch et al. (2018) sample of 45 galaxies, which includes 30 AGNs and 15 starburst galaxies, it appeared that 15 out of the 30 AGNs and the extra two galaxies (NGC 613 and ESO 420-613) are possible candidates for hosting a jet-driven molecular outflow while 9 out of 30 are AGNs with radio emission probably emanating from starburst regions. The rest are galaxies that we didn't have enough information about, for a conclusion to be reached. These indications are summarized in Fig.2.1. In this plot one can see that galaxies with a radio jet can efficiently explain the outflows, instead of momentum boosting due to radiation, since they appear on or over the $v\dot{M} \sim 20L_{AGN}/c$ line.

FIGURE 2.1: Outflow's momentum rate relation with the total photon momentum output of the galaxy. The dashed lines denote the different values of the ratio of outflow's momentum rate over AGN luminosity. The arrows denote upper limit values.
The first category refers to galaxies with jet-driven molecular outflows, the second one to galaxies with ionized jet-driven outflows and the third category refers to galaxies with potentially jet-driven molecular outflows (adapted from Fluetsch et al., 2018)

2.2 ARC sample

Having strong evidence for the viability of the radio mode in galaxies with molecular outflows, motivated the design of a new survey for the detection of molecular winds in radio galaxies, called the ALMA Radio-Source Catalogue project. This project was benefited from the wealth of the archival data of the Atacama Large Millimeter Array (ALMA). Out of all the radio galaxies with CO spectral coverage included in our team and ALMA's archive we selected only 70 in order for them to be representative of the NVSS catalog with a flux limitation at 0.4Jy. The purpose of this survey is to perform molecular gas content statistics at different redshifts, to derive the occurrence frequency and properties of winds in radio galaxies, to derive the properties of radio galaxies (luminosity and mass functions) and finally to evaluate the role of radio activity in the evolution of the host galaxy. The latter is going to be achieved by fitting the SED of the galaxies, in order to obtain the needed physical parameter, which is what my thesis is focused on.

For the ARC project we use our own data and data from the ALMA archive which includes both target sources as well as calibrator sources. To get access to the observational data we used the python astroquery package to mine through ALMA archive for every observation made for each object in ARC. Mining was conducted using the astroquery package, which searched from a list of alternative names for each object given by ARC. For the mining through the ALMA archive the Alma.query object function was used. For unregistered sources we searched in a radius of 2 arcsec around its registered sky coordinates (M.Papachristou PhD thesis).

When performing interferometry one needs to use a calibration method to convert the raw data to the correct flux of the targeted source. So the technical staff of the telescope selects a group of sources called calibrators that, as their name denotes, alleviate the problem of calibration and correction of raw data. Therefore, for the purposes of our project we get advantage of the ALMA source calibrators catalogue, which is openly accessed after two years of the observations of each source. This catalogue includes galactic populations like dusty galaxies, blazers, and many other that are bright in the mm/sub-mm regime. Since our goal is to study the impact of radio jets on the gas, we need galaxies that are bright in the radio and representative of a radio catalogue.

Managing a sample of galaxies representative of a radio catalogue requires the selection of the most appropriate radio catalogue as well as the most appropriate sample. In order to do the former we compare the galaxies included in the CO-ARC (sample of galaxies from the ALMA archive that also have CO spectral coverage) with each radio catalogue (6C at 151MHz, NVSS at 1.4 GHz, Parkes Radio Sources Catalogue at 2.7GHz and at 4.8 GHz, MIT-Green Bank 5GHz Survey). Eventually, we select the radio catalogue with the smallest D-statistic according to the Kolmogorov and Smirnov test, which is the NVSS catalogue (Fig. 2.2). After choosing the most suitable radio catalogue as the parent sample, the next step is to select a subsample of the CO-ARC that would be as small as possible and representative of the selected radio catalogue at the same time. To do so, we apply a specific criterion (thoroughly explained in M.Papachristou PhD thesis) denoting that D distance should be lower than 0.2. By taking into consideration this criterion the resulting sample is of size 70 with D-statistic value 0.15 (Fig. 2.3). So in this way we managed to generate a sample representative of the NVSS catalogue from a huge sample of galaxies bright at the mm/sub-mm regime.
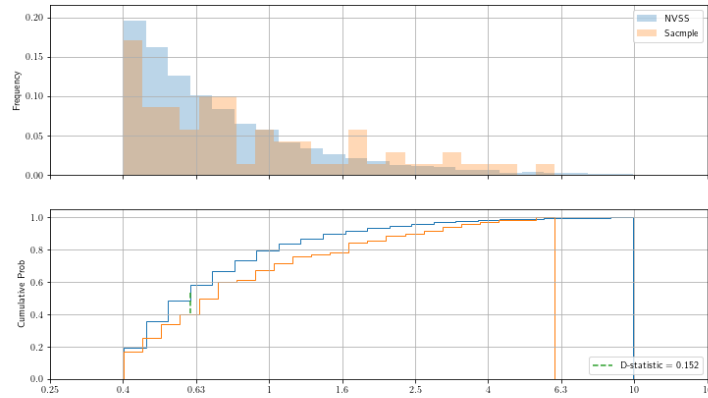
FIGURE 2.2: *top*: Comparison of CO-ARC flux distribution with the NVSS radio survey, *bottom*: Comparison of CO-ARC cumulative flux distribution with the NVSS radio survey, flux limited at 0.4Jy (M.Papachristou PhD thesis)
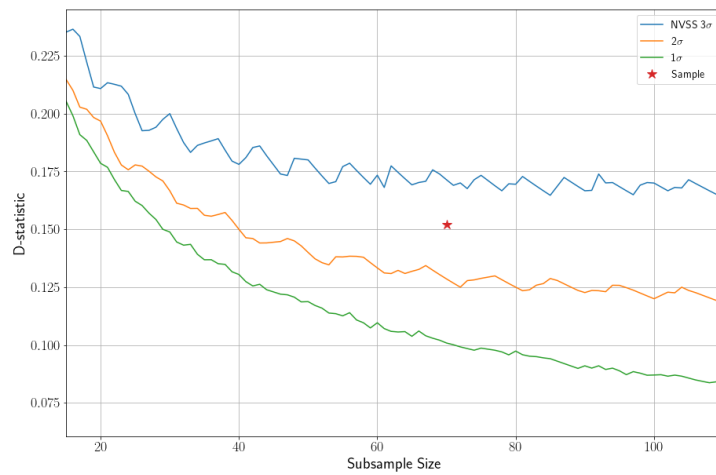
FIGURE 2.3: The position of the our final 70-galaxies sample in the D-statistic - sample size plot (M.Papachristou PhD thesis)

Chapter 3

Modeling the SEDs of galaxies

When having information about the spectral energy distribution (SED) of a galaxy one of the most used techniques to extract physical information about the galaxy is performing SED-fitting. In order to do that one needs to describe and implement correctly in the code all the components that create the galaxy's total SED. Significant prerequisite is firstly knowing the components creating the SED, secondarily the physics behind each one of the them and finally simulating each component in the most accurate and physical model possible.

Normal galaxies are composed of a central supermassive black hole and around it stars, gas and dust orbit. Active galaxies, additionally to these components, hold a radio jet emanating from somewhere close to the central black hole and extending up to pc or kpc scales. Each galactic component radiates in different wavelengths, because of different physical processes, composing the SED of the galaxy (Fig. 3.1). The SED of each galaxy depicts almost every physical property of the system so by studying it we can obtain significant information about the physics of the galaxies.

3.1 Stars

In order to create a set of stellar templates that will represent the stellar component in a galactic SED, we need to add a set of SSPs, an IMF, a SFH and a dust attenuation law (see Section 3.2). Afterwards we run it with a special software (there are several codes for this purpose, here CIGALE is used Boquien et al. (2019)) and the final step is to convert
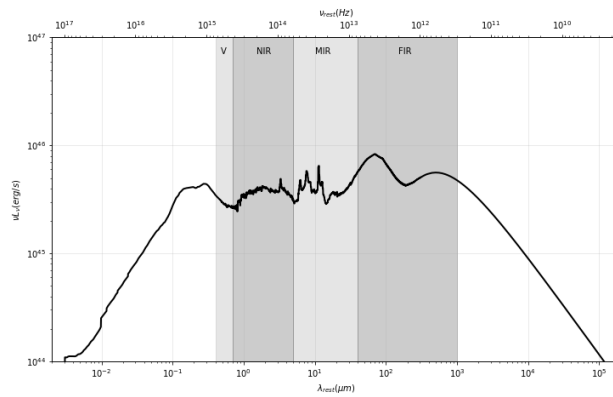
FIGURE 3.1: SED of a quasar

the model flux into rest-frame luminosity. The model generated by the codes is given in observed-frame flux. So, because of the Doppler effect we need to correct the observed flux and frequency using the redshift (z) of the galaxy.

$$\nu_{rest} = (1 + z)\nu_{obs}$$
$$F_\nu^{(rest)} = \frac{F_\nu^{(obs)}}{1 + z} \tag{3.1}$$

Knowing the redshift of the galaxy we can obtain the luminosity distance D_L. The next and final step is to transform the flux to luminosity using eq. 3.2

$$\nu_{rest}L_{\nu,rest} = 4\pi D_L^2(\nu_{rest}F_{\nu,rest}) \tag{3.2}$$

The shape of the spectrum of a single star is determined by the star's temperature, age and metallicity while the evolution of the stellar spectrum is defined by the star's mass (Fig. 3.2). More specifically, Wien's displacement law ($T\lambda_{max} = 2.9 \cdot 10^3$ $[\mu m K]$) shows that the surface temperature of the star defines the wavelength at which the spectrum peaks, the shorter the peak-wavelength the higher the temperature. The temperature factor is affected by both the age and metallicity of the star. Young and metal poor stars tend to be bluer hence warmer while old and metal rich stars tend to be redder hence cooler. Additionally, the stellar mass determines the initial placement of the star in the HR diagram and eventually the rate of its evolution (Fig. 3.3).

In a galaxy, although, there are many stars of different temperatures, metallicities, ages and masses so we need to classify them in groups according to their properties. A group of
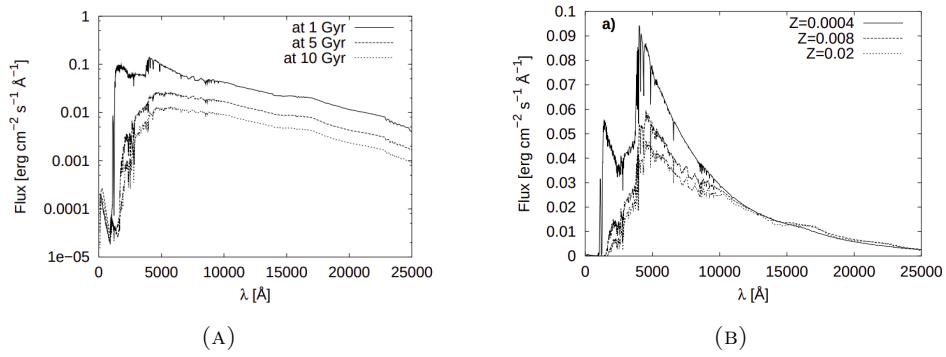
FIGURE 3.2: (A): Age evolution causes peak of the spectrum move to the right while the decreasing temperature causes the reducing amplitude via Stefan-Boltzmann's law, (B): Metallicity effects on the spectral evolution (Schulz et al., 2002)
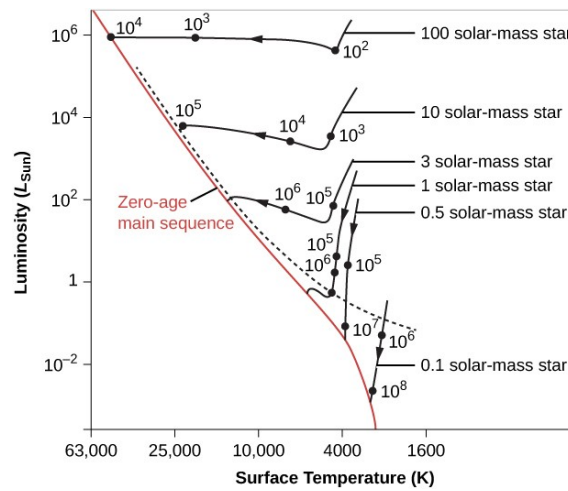
FIGURE 3.3: Each track shows the different timescale that stars of different masses need to evolve (source).

coeval stars at a single metallicity and abundance pattern comprises the so called Single Stellar Population (SSP) which describes the evolution in time of its SED. To construct an SSP three input parameters are needed. Firstly, an Initial Mass Function (IMF) which defines the number of stars and their masses, isochrones which are curves that describe the evolution of the stars and a set of stellar spectra which define the shape of spectrum of each star according to its metallicity (Fig. 3.4).

3.1.1 IMF

The initial mass function shows the initial distribution of stellar masses. This information is important because it defines the starting point of the evolution of a single stellar population as well as the timescale needed for the stellar population to evolve. Mass is
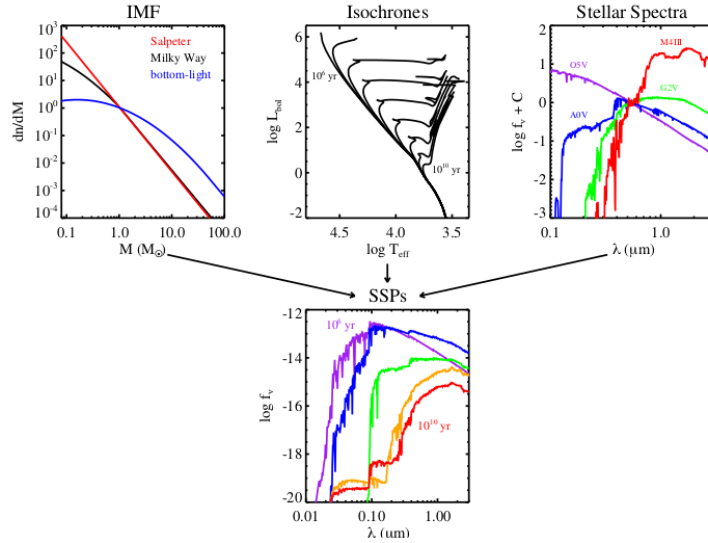
FIGURE 3.4: Construction of an SSP model (taken from Conroy, 2013)

not a directly observed quantity, like flux for example. Therefore, the mass function is obtained by observing the integrated light of the stars and using theoretical relations of mass with age and light. In this way the light information is converted to mass information and evenutally the mass function is structured. The first extensive study over the establishment of a global IMF was made by Salpeter (1955). This IMF is described by a function of the following form

$$\frac{dN}{dM} \propto M^{-2.35} \tag{3.3}$$

Throughout the years telescopes with better resolution were developed, both ground-based and space-based, making them more effective in observing smaller and fainter objects. Dwarf stars live close to Hubble time or longer, since the smaller the radius of a star the longer its life duration. They provide the majority of the galactic stellar content so it is vital to include them while modeling a mass function. That is why the buildout of more effective telescopes revealed a different IMF shape than the so far known one. Specifically, observations near the solar neighborhood resulted in an IMF that deviated from the Salpeter IMF, for masses below $1M_\odot$ (Reid et al., 1999). So, by exploiting the potential of the new and strong telescopes as well as the improved theoretical models, several IMFs were developed.

Kroupa (2001) implemented all the contemporary observations of dwarf stars and broke the mass function down into two components, the galactic-field stars and the globular

cluster stars. The result showed that above $1M_\odot$ the slope of the power law agrees with the Salpeter IMF while for mass belowe $1M_\odot$ there are variations in the slope of the power-law (eq. 3.4).

$$\xi(M) \propto \begin{cases} M^{-0.3} & M < 0.08M_\odot \\ M^{-1.3} & 0.08M_\odot < M < 0.5M_\odot \\ M^{-2.35} & 0.5M_\odot < M \end{cases} \qquad (3.4)$$

Furthermore, Chabrier (2003) added a correction for the unresolved binary systems and divided the study of the mass function into the galactic field stars, the galactic spheroid stars and the stars in the globular clusters. The result was a smoother IMF than the one Kroupa presented, with a continuously changing slope below $1M_\odot$ (eq. 3.5).

$$\xi(logM) \propto \begin{cases} 3.6 \cdot 10^{-4} exp(-\frac{[logM - log0.22]^2}{2 \cdot 0.33^2}) & M < 0.7M_\odot \\ M^{-2.35} & M > 0.7M_\odot \end{cases} \qquad (3.5)$$

It is important to pick the most suitable IMF because it determines the mass-to-light (M/L) normalization, hence the stellar masses, and the rate of luminosity evolution for a passively evolving population. In Fig. 3.5 we can see the differences between the three IMF models.

In this work we selected the Chabrier IMF since it is the most recent one and includes more up to date corrections and theoretical evolutionary models.
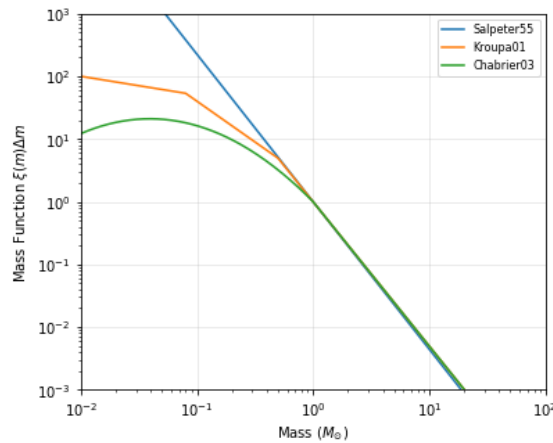
FIGURE 3.5: The initial mass functions of Salpeter, Kroupa and Chabrier

3.1.2 SSPs

As it was mentioned above, an SSP is constructed by adding an IMF, a set of isochrones, and stellar spectral libraries. There are several studies dedicated to the construction of SSP models (Leitherer et al., 1999; Bruzual, Charlot, 2003; Maraston, 2005; Vazdekis et al., 2010). In this work the set of SSPs that is used is the one presented by Bruzual, Charlot (2003) (Fig. 3.6) because they are the most used in the literature so it was easier to test the accuracy of my results by comparing them with similar studies in the literature.
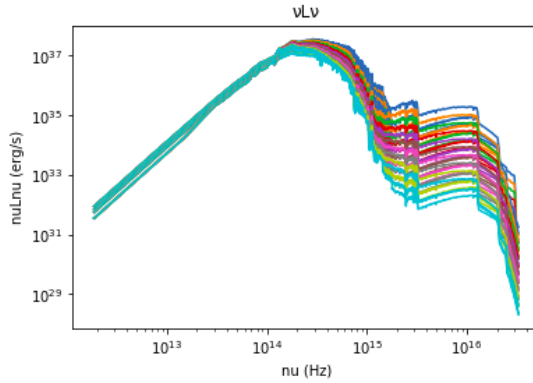
FIGURE 3.6: Bruzual, Charlot (2003) templates

While galaxies evolve secularly they accrete and expel gas. This leads to increasing or decreasing star formation leaving eventually the galaxy with stellar populations of different ages. In young galaxies there are still young, massive and short-lived stars. These stars are very luminous and hot and according to Wien's law they mainly radiate in UV wavelengths. So the spectrum of a young stellar population ($t < 10^6 yr$) appears brighter in UV and less brighter in IR wavelengths. While the time passes ($10^6 yr < t < 10^7 yr$) the massive stars evolve to red supergiants which are less hot hence their radiation peaks at NIR. At the same time the UV luminosity gets dimmer since there are less massive young stars. As the galaxy gets older ($10^8 < t < 10^9 yr$) AGB stars appear increasing the NIR luminosity. UV luminosity keeps dropping since the turnoff mass keeps decreasing. Finally at ages $t > 10^9 yr$ red giants account for the most of the NIR light, while accumulated white dwarfs and AGB stars increase the FUV light. At $4000 \mathring{A}$ we can observe a spectral break which becomes prominent after a few 10^7 years. It is caused by a strongly changing opacity of stellar atmospheres at this wavelength. The evolution of the SED of a single stellar population is depicted in Fig. 3.7. Age is one of the most defining factor for the shape of the stellar population spectrum. Therefore, since it is imprinted in the final

stellar component, it is important to have the age information of each stellar population comprising the galaxy. This information is given by the star formation history (SFH) of a galaxy.
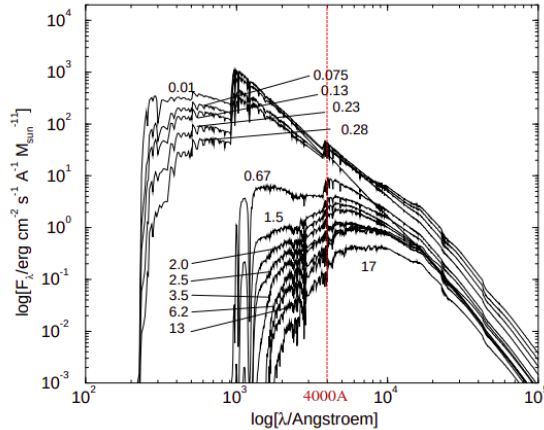
FIGURE 3.7: Spectral energy distribution of a simple stellar population with mass $10^{11} M_\odot$ and sollar metallicity evolving from an age of 0.01 Gyrs to 17 Gyrs (Kneiske, Mannheim, 1999)

Since SSPs include stars of specific ages in order to represent the whole stellar population of a galaxy we need to combine the existing SSPs with a given SFH. In this way we get the final stellar population of the galaxy that can simulate the stellar component in the SED of the galaxy.

Constraining the SFH of a galaxy is not a trivial task, in the contrary it is a highly degenerate problem. That is why most studies have adopted simple formulas to reproduce the variations of star formation rate (SFR). Some of these formulas are the following:

- **Decaying exponential**: in this model we assume that there was an episode of star formation in the beginning and since then the SFR started being reduced exponentially (Fig. 3.8) (e.g. Boquien et al., 2019; Lower et al., 2020). The corresponding formula is

$$SFR(t) \propto e^{-t/\tau_o} \quad \text{if} \quad t_o < t < t_1$$

where τ_o is the e-folding time.

- **Delayed SFH**: in this module we assume that the onset of the star formation was delayed and didn't happen suddenly like the previous case (Fig. 3.9) (Sandage 1986,
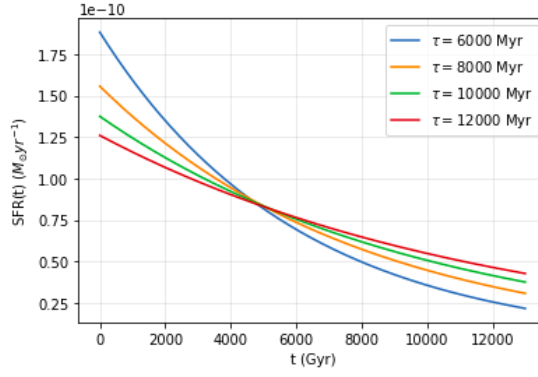
FIGURE 3.8: Exponentially decreasing SFH

e.g. Boquien et al. 2019; Lower et al. 2020). The formula for this module is

$$SFR(t) \propto \frac{t}{\tau^2} e^{-t/\tau}$$

where τ is the e-folding time. Early-type galaxies can be described by small values of τ while late-type galaxies by large values.

(A)

(B)
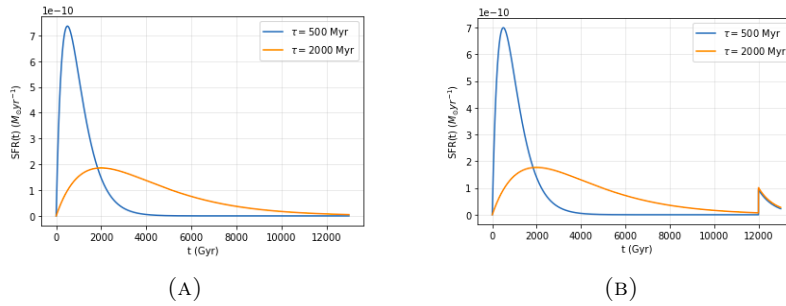
FIGURE 3.9: [A]: Delayed SFH with only one star formation episode, [B]: Delayed SFH with two episodes of star formation

- **Periodic**: In this module it is presumed that star formation episodes are repeated in a periodic way. The formation episodes can be of three different forms, exponential, delayed or rectangular (Fig. 3.10) (e.g. Boquien et al., 2019).

However many numerical simulations have been made in order to improve the existing formulas and approach more realistically the star formation episodes of different types of galaxies (Pacifici et al., 2012; Boquien et al., 2014).
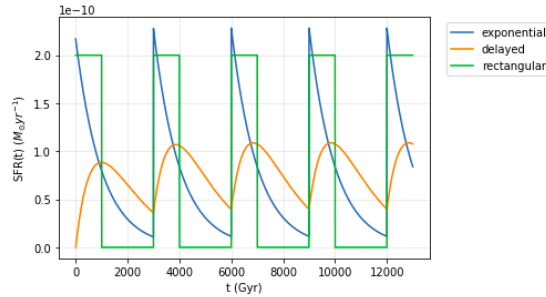
FIGURE 3.10: Periodic SFH

Among the above formulas used in the literature, in this work we selected the "delayed" SFH module (Fig. 3.9 (A)) or the "delayed" module with a second episode of star formation (Fig. 3.9 (B)). We chose the "delayed" module in order to avoid extra parameters that would make our model even more complicated with no apparent reason.

3.2 Dust

The interstellar dust exists in galactic disks, spiral arms and tidal tails. In its dense regions there is immense star formation, in particular in HII and photo-dissociation regions (PDRs) or molecular clouds. The dust has a dual role in defining the shape of the galactic SED. On the one hand dust absorbs starlight, from UV through NIR wavelengths, and on the other hand it re-emits it in MIR-FIR. In order to construct a model simulating the dust attenuation or emission we need to make some determinant assumptions about the nature of the dust. That is its composition, geometry and size distribution.

3.2.1 Dust Attenuation

The fact that starlight is attenuated by dust should not be confused with the extinction. These two processes are slightly different. Extinction occurs when the observed source is behind the dust, in the background. In this case the reduced light reaching in the observer's eye has been both absorbed and scattered off the line of sight. But when the dust is in between the observed sources the light can be either scattered off or towards the line of the observer's sight (Fig. 3.11). The way that the starlight is attenuated can be described by many different laws, depending on the kind of galaxy we are studying. In this section I am going to refer to the two most common ones in the literature.
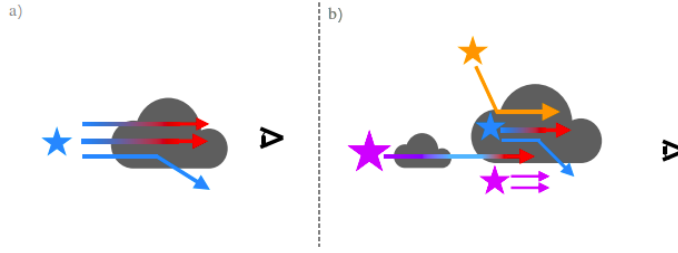
FIGURE 3.11: Left: Dust extinction, Right: Dust attenuation (Salim, Narayanan, 2020)

The first one is the law presented in Calzetti et al. (2000). This law was obtained after the examination of eight low-redshift starburst galaxies ($z < 0.03$), with bright UV radiation, intrinsic color excess in the range $E(B - V) = 0 - 0.7mag$, and SFRs in the range $0.2 - 0.55 M_\odot yr^{-1}$. By observing the UV part of the galactic SED one knows the attenuated stellar emission, while by observing the FIR part of the SED one can estimate the dust emission. There are relations that convert the FIR flux to dust mass, so using them can lead to the calculation of the total dust emission. Since the dust emission is equal to the total stellar emission attenuated by the dust, knowing both the dust emission and the stellar attenuated emission one can yield the total stellar energy absorbed by the dust. Following this logic path Calzetti proposed that the observed flux is given by the formula:

$$F_{obs}(\lambda) = F_{int}(\lambda) 10^{-0.4A_\lambda} \tag{3.6}$$

with

$$A_\lambda = k(\lambda) E(B - V)$$

and

$$k(\lambda) = \begin{cases} 2.659(-2.156 + \frac{1.509}{\lambda} - \frac{0.198}{\lambda^2} + \frac{0.011}{\lambda^3}) + 4.05, & 0.12\mu m \leqslant \lambda \leqslant 0.63\mu m \\ 2.659(-1.857 + \frac{1.040}{\lambda}) + 4.05, & 0.63\mu m \leqslant \lambda \leqslant 2.20\mu m \end{cases}$$

The other most usual attenuation law is the one presented by Charlot, Fall (2000). This law can describe starburst galaxies, hence galaxies with strong star formation, but with suitable adjustments of its parameters it can describe more quiescent galaxies as well. The different approach of this law, compared to Calzetti's law, is that light from young and old stars is attenuated differently. This is because the light from old stars while traveling towards the observer encounters only ISM dust but younger stars are still embedded in
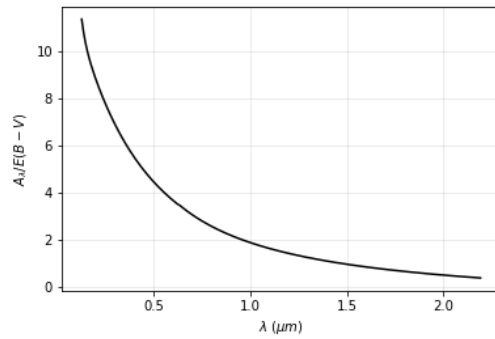
FIGURE 3.12: The curve of the Calzetti attenuation law

their birth cloud so their light gets attenuated by both their birth cloud and ISM dust (Fig. 3.13). This is modelled by the use of two different power-law attenuation curves, one for younger stars ($t_{age} < 10^7$ Myr) and one for the older stars ($t_{age} > 10^7$ Myr) (3.7).

$$A(\lambda) \propto \lambda^{\delta_{ISM}}, \quad A(\lambda) \propto \lambda^{\delta_{BC}} \tag{3.7}$$
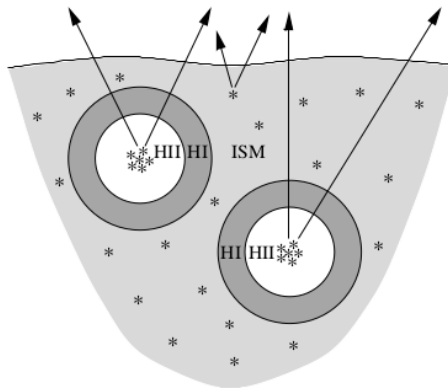
FIGURE 3.13: Schematic representation of the dust geometry in birth clouds and ISM (Charlot, Fall, 2000)

There is a range of values to pick for the two slopes depending on the type and age of galaxy that one aims to model. The most simple recipe recommended, though, is to set both slopes at $\delta_{ISM} = \delta_{BC} = -0.7$ and just change their normalization (recommended in Charlot, Fall, 2000). For younger stars the normalization will be lower while for older stars it will be higher, solving in this way the problem of different dust attenuation for different ages.

3.2.2   Dust Emission

All the energy absorbed by the dust is re-emitted in MIR-FIR wavelengths. Generally, dust emission can be classified into three broad components. In mid-IR (around $8\mu m$) the emission is dominated by polycyclic aromatic hydrocarbon (PAH) bands. In wavelengths longer than $8\mu m$ but shorter than $100\mu m$ the emission is dominated by the small and warm dust grains emission while over $100\mu m$ emission from cold and big dust grains becomes prominent.

In order to model the dust emission we need to deduce the intensity of the starlight heating the dust as well as the composition, size distribution and geometry of the dust.

The modeling of the dust emission is still an active field of research. Although, there have been developed several models that can adequately explain the observations. Here I am going to present two of the most important ones.

Dale, Helou (2002) created empirical IR templates based on nearby star-forming galaxies. Their model includes three dust components: large grains that are in thermal equilibrium, semi-stochastically heated small grains, and PAHs stochastically heated by individual ultraviolet or optical photons. The way of parameterizing the dust models is by correlating the heated dust mass (dM_d) with the intensity of the radiation field (U) heating it (eq. 3.8).

$$dM_d(U) \propto U^{-\alpha}dU \tag{3.8}$$

These models are semi-empirical because they were constructed based on observations of the dust emission in the Milky Way. The resulting SEDs were normalized so that U=1 correspond to the local interstellar radiation field, while the range of the radiation field is $0.3 < U < 10^5$. So the final emission is the superposition of different radiation fields. The relative contributions of the different radiation fields are defined by the parameter α. This model is one of the most used in the literature since it is simple and uses one easy-to-interpret parameter.

The model presented by Draine, Li (2007) also uses a dust mixture of amorphous silicate and graphite grains, and PAH. Although the main difference arise in the modeling of the radiation field. They separate the dust emission in two components. The first one describes how the dust is heated by the general stellar population hence by a single radiation field (U_{min}). The second one describes how the dust is tightly linked to the

star-forming regions. In this case the illuminating radiation field varies within the range $U_{min} < U < U_{max}$ and is regulated by a power-law with slope α. The factor $1 - \gamma$ defines the fraction of the dust mass exposed to starlight of intensity U_{min}, while γ defines the rest of the radiation heating the dust. The modeling formula is denoted by eq.3.9.

$$\frac{dM_{dust}}{dU} = (1 - \gamma)M_{dust}\delta(U - U_{min}) + \gamma M_{dust}\frac{\alpha - 1}{U_{min}^{1-\alpha} - U_{max}^{1-\alpha}}, \quad a \neq 1 \qquad (3.9)$$
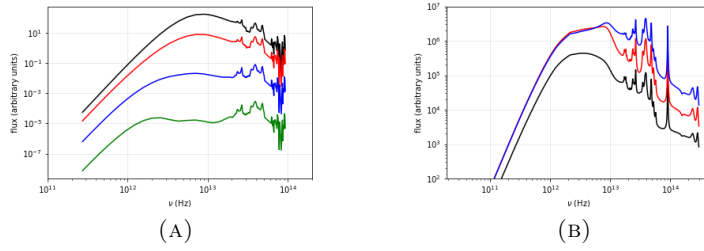
FIGURE 3.14: [A]: Dale, Helou (2002) templates, [B]: Draine, Li (2007) templates

The models generate templates in units of flux as if the galaxy is observed from a distance of 10pc. So I need to convert the model flux into rest-frame luminosity (eq. 3.10).

$$L_{\nu,rest} = 4\pi D_L^2 F_{\nu,model} \quad \text{with} \quad D = 10pc = 3 \cdot 10^{19}cm \qquad (3.10)$$

3.3 Supernovae

Starburst galaxies have strong star formation which means big amount of supernovae events. Supernova explosions result in the creation of supernova remnants (SNR). Their role is very important for the understanding of the galaxies. First of all, they release a great deal of energy in the ISM heating it up, they also distribute heavy elements throughout the galaxy, and finally they accelerate electrons, protons, and ions via Fermi acceleration process.

The accelerated electrons reach relativistic velocities so when they enter the SNR magnetic field in the appropriate angle (pitch angle) the radiate through synchrotron radiation (see sec. 3.4).

Some evolved SNRs that are embedded in a dense ISM environment produce thermal bremsstrahlung radiation, other than synchrotron radiation. Bremmstrahlung radiation

is the radiation produced when a charged particle (electron) passes by an ion causing its trajectory to bend, hence its velocity to accelerate and energy is radiated away. By thermal bremsstrahlung we mean the case where there is a distribution of energies of the charged particles and a range of approaching distances b (see Fig. 3.15). This mechanism is also the reason why the there is an observed radio-L_{IR} relation in starburst galaxies (Helou et al., 1985).

Synchrotron and bremsstrahlung radiation from SNRs are significant in the radio regime (Urošević, Pannuti, 2005; Onic et al., 2012). Especially, when bremsstrahlung is combined with synchrotron the spectrum appears flatter, as it is shown in the SED of a typical starburst galaxy, M82 (Fig. 3.16).
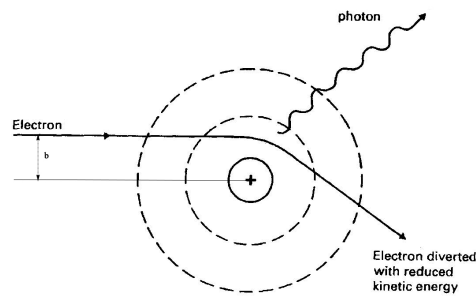
FIGURE 3.15: Bremsstrahlung radiation scheme
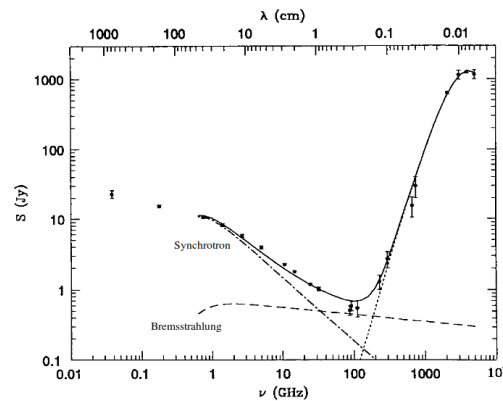
FIGURE 3.16: The radio and far-infrared spectrum of the nearby starburst galaxy M82

The SNRs is more possible to appear in starburst regions where there are also great amounts of dust. That is why the contribution of the SNRs in the radio regime of the galactic SED is added as en extension to the dust models (Dale, Helou, 2002). These extended templates are presented in Dale et al. (2014) and are shown in Fig. 3.17. So, by

using them we can disentangle the radio emission coming from the SNRs and the radio jet (see sec. 3.4).
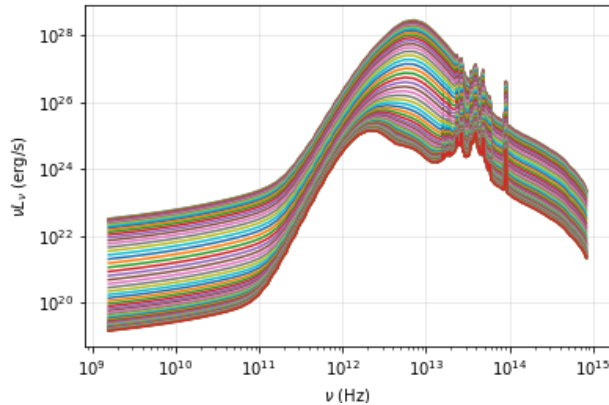
FIGURE 3.17:   FIR-mm templates, including dust emission and synchrotron and bremsstrahlung emission from SNRs (Dale et al., 2014)

3.4   AGN

3.4.1   Big Blue Bump

Active galaxies host a supermassive black hole in their centre, which accretes the surrounding material. Because of angular momentum conservation this process leads to the formation of an accretion disk. If the gas in the disk is optically thin it emits energy depending on the disk's temperature which in turn depends on the radial distance from the galactic center. So eventually, the radiation from the accretion disk is the sum of many black bodies of different temperatures (eq.3.11). The resulting spectrum stands out in the galactic SED and peaks mainly in the blue band that is why the accretion disk emission is also called big blue bump emission (hereafter BBB).

$$F_\nu \propto \frac{2h\nu^3}{c^2} \frac{1}{e^{h\nu/kT(r)} - 1} \tag{3.11}$$

$$\text{with} \quad T(r) = \left[\frac{3GM\dot{M}}{8\pi\sigma_{SB}} \left(1 - \sqrt{\frac{r_{in}}{r}} \right) \right]^{1/4} r^{-3/4} \tag{3.12}$$

r is the distance from the center of the galaxy, r_{in} is the closest to the AGN radius, $\dot{M}$ is the accretion mass rate and σ_{SB} the Stefan-Boltzmann constant. The above formula is

for the simplest case of an accretion disk that is optically thin and that radiates all the energy created by the accreting mass.

However, in the case of optically thick disks, there are extra procedures that should be taken into account like non-LTE effects (Local Thermal Equilibrium), Comptonization, and interaction between the disk and X-ray producing regions. Many studies, throughout the years, have been dedicated to model the emission of a geometrically thin and optically thick accretion disk (Hubeny et al., 2000; Lodato, Bertin, 2001; Slone, Netzer, 2012). In this work the accretion disk model used is the one presented in Richards et al. (2006). It is an empirical template which is obtained by averaging the SEDs of 259 type 1 quasars. We selected this one because it is a simple model and easily parameterized (as explained in the next paragraph). However, there is room for improvement by adding more recent models, like the one presented in Slone, Netzer (2012).

The BBB emission can be extincted by the dust along the line of sight or be totally obscured by the AGN torus. For the case of type 1 AGNs we can use one of the existing extinction laws: Allen (1976) for the Milky Way (MW), Seaton (1979) for the MW, Fitzpatrick (1986) for the Large Magellanic Cloud (LMC), Prevot et al. (1984) and Bouchet et al. (1985) for the Small Magellanic Cloud (SMC). In this work, out of all the above laws Prevot et al. (1984) is selected since previous studies showed that it is the most appropriate law for type 1 AGNs (Hopkins et al., 2004). The reddening law is described by equation 3.13. So, starting by a single empirical template we parameterize the BBB model by the reddening factor.

$$
\begin{aligned}
F_{osb}(\lambda) &= F_{int}(\lambda) \cdot 10^{-0.4A_\lambda} \\
A_\lambda &= k(\lambda)E(B-V)_{bbb} \\
k(\lambda) &= 1.39(10^{-4}\lambda)^{-1.2} - 0.38
\end{aligned}
\tag{3.13}
$$

3.4.2 AGN torus

In some AGNs there were observations of both narrow and broad emission lines while in other only narrow emission lines. The solution to this dichotomy was given by the existence of a toroidal region around the AGN. This region is assumed to consist of dust
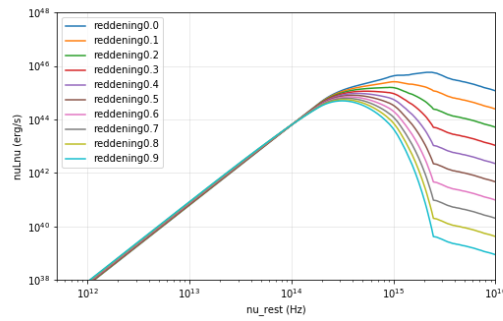
FIGURE 3.18: Big blue bump templates as they appear after applying the extinction law

and molecular clouds. So depending on the angle of observation the broad lines are obscured by the dusty torus (Fig.3.20).

Part of the torus consists of dust, so the dust gets heated by the absorbed accretion disk radiation and thermally radiates it back. This is the same as the re-radiation of the absorbed starlight by ISM dust mentioned in sesction 3.2. The dusty torus emission dominates the NIR and MIR wavelengths, while around $10 - 18\mu m$ emission and absorption features are prominent because of the silicate composition of the dust. The torus emission is abruptly cut off at around $1\mu m$ where the bbb bump emission starts being significant.
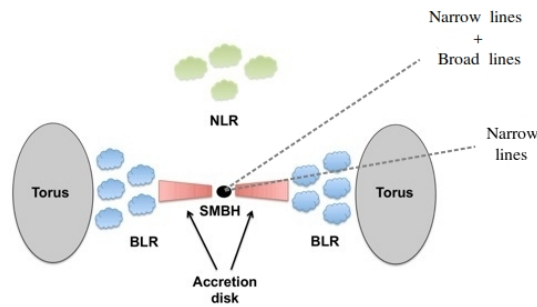
FIGURE 3.19: AGN unification scheme

Since the dust thermally radiates, temperature is one main factor defining the shape of the SED and the position of the peak, especially the higher temperatures. Torus temperatures can vary from ISM-like temperatures up to 1500K. Lower temperatures come from the outer parts of the torus, while higher temperatures are succeeded at the smallest radius. The smallest radius where dust can survive is called sublimation radius (r_{sub}) and can vary depending on the size and composition of the dust as well as on the AGN luminosity (L_{AGN}). The higher the AGN luminosity the higher the temperature close to it, so

the sublimation radius increases. The sublimation radius of the dust can be estimated by reverberation mapping (Peterson, 1993; Netzer, 2015). Torus dust is composed of graphite and silicate grains, which have different temperature resistance. Graphite grains can exist in higher temperatures than silicate grains so $r_{sub}^{(graph)} < r_{sub}^{(sil)}$. Also the size of the grains can affect the sublimation radius because larger grains are more resilient than smaller grains, so they can survive higher temperatures hence smaller radii.

Since first proposed, our view of the torus has evolved enormously and so have the models. Initially the models used uniformly distributed dust in the torus (e.g. Fritz et al. 2006) but it was later understood that a clumpy distribution is more appropriate (Hoenig, Kishimoto, 2010). Even newer models (García-González et al., 2017) implemented a more physical approach for the dust sublimation radius as well as anisotropic AGN emission (Fig. ...), bringing the torus emission closer to reality.
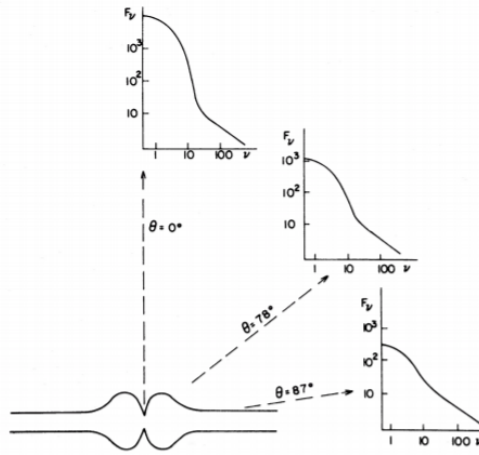
FIGURE 3.20: At different angles with respect to the accretion disk the UV radiation intensity varies. The adopted formula is $\propto \frac{1}{3}cos(i)(1+2cos(i))$ (taken from Netzer, 1987)

CAT3D is the model presented and used in this work, initially presented by Hoenig, Kishimoto (2010) and improved by García-González et al. (2017). This model generates AGN torus templates by solving the radiative transfer equation for a ray of radiation propagating through a torus consisting of dust clouds. There are seven input parameters defining the shape of the final torus templates. These are:

– power-law index a: defines the radial distribution of dust clouds along the line of sight

$$N_{clouds} \propto r^a$$

- N_o: number of clouds along the line of sight

- θ_o: the half-covering angle of the torus

- τ_ν: optical depth of each cloud

- R_{out}: the outer radius of the torus

- R_{cl}: the radius of each cloud

- i: inclination

The scheme in Fig. 3.21 shows the physical quantities corresponding to some of the above parameters.
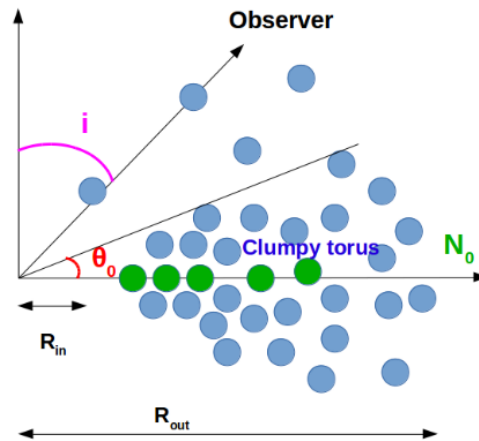
FIGURE 3.21: AGN torus scheme: explanation of 4 of the CAT3D parameters (García-González et al., 2017)

Flatter cloud distributions (meaning a value closer to zero) produce redder SEDs while steeper distributions result in bluer SEDs. This is because when the cloud distribution is flatter it means that there are many clouds in the outer torus radii. So the majority of the dust is cool hence radiates in longer wavelengths (redder wavelengths). On the other hand steeper cloud distribution means more clouds at small radii where the temperature is higher hence the dust emission peaks at smaller wavelengths (bluer wavelengths). The power-law index, a, also affects the strength of the silicate feature, as well as the number of clouds does. When a=-1.5 silicate emission is always prominent, although for the rest of power-law index values the silicate emission depends on the number of clouds (N_o) along the line of sight. The inclination is also a parameter that can cause deep silicate

absorption features together with N_o. Summing up, the value of α parameter has a strong effect on the shape of the SED while N_o and i values affect the silicate features strength.

The different templates generated by different set of parameters are shown in Fig. 3.22.
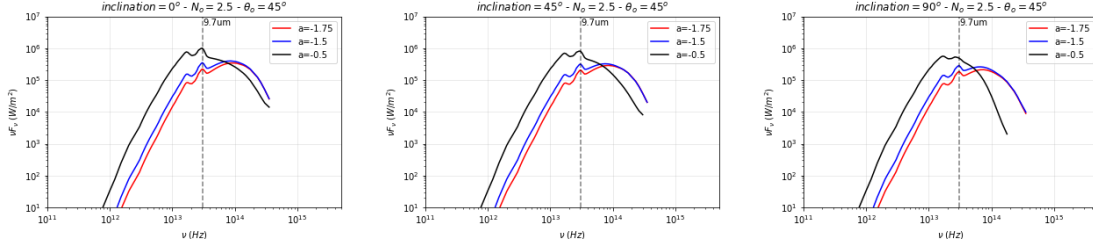
FIGURE 3.22: Set of torus templates generated using the CAT3D model, the silicate feature at $9.7\mu m$ is depicted with the grey dashed line. Parameters values: $i = 0^o, 45^o, 90^o, N_o = 2.5, \theta_o = 45^o, \alpha = -0.5, -1.5, -1.75$

In order to use the CAT3D templates for SED-fitting purposes we need to convert the flux given by the model into real flux, since the model creates the flux as if it is observed at distance equal to the sublimation radius (eq.3.14) and eventually into rest-frame luminosity (eq.3.15).

$$\left.\begin{aligned}(\nu F_\nu)_{obs} =&(\nu F_\nu)_{model} \left(\frac{r_{sub}}{D_L}\right)^2 \\ r_{sub} =&r_{sub,o} \left(\frac{L_{AGN}}{10^{46}erg/s}\right)^{1/2}\end{aligned}\right\} \Rightarrow (\nu F_\nu)_{obs} = (\nu F_\nu)_{model} \left(\frac{r_{sub,o}}{D_L}\right)^2 \left(\frac{L_{AGN}}{10^{46}erg/s}\right)$$

$$(3.14)$$

$$\nu L_\nu = 4\pi D_L^2 (\nu F_\nu)_{model} \tag{3.15}$$

with r_{sub} the dust sublimation radius and D_L the luminosity distance of the galaxy. The $r_{sub,o}$ value depends on the dust which is used in the models and provided in the model description.

3.4.3 Radio jet

Last but equally important component of the AGN is the emission emanating from the jet. The jet radiation can span the full range of the electromagnetic spectrum, but for each band a different physical process is responsible. Specifically, the jet radiation from

the radio though the X-rays band accounts for synchrotron radiation (Westfold, 1959) and in some cases bremmstrahlung radiation as well, while the gamma rays spectrum is dominated by the Inverse Compton radiation.

When an electron travels with relativistic velocity ($\beta = v/c$) in a magnetic field it radiates energy according to Larmor formula. The total emitted radiation, which is equal to the total energy losses of the electrons, is given by equation 3.16. One basic condition, though, for the relativistic electron to radiate is the pitch angle to not be zero. Pitch angle is the angle between the particle velocity and the magnetic field.

$$P = \frac{4}{3}\sigma_T c \beta^2 \gamma^2 U_B \tag{3.16}$$

where σ_T is the Thomson cross section, β the velocity of the electrons, γ the Lorentz factor and $U_B = \frac{B^2}{8\pi}$ the magnetic energy density.
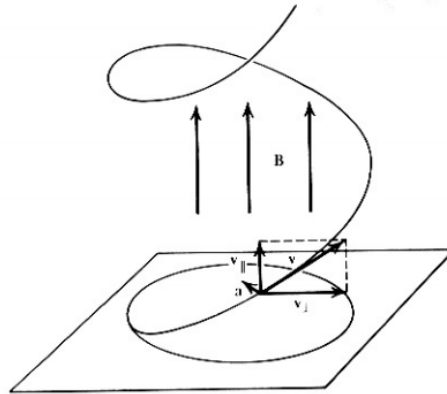
FIGURE 3.23: Schematic repserantation of the synchrotron process (Rybicki, Lightman, 2004)

The spectrum of a monochromatic electron moving with a Lorentz factor γ in a magnetic field B is proportional to the synchrotron emissivity (j_{syn}) given by equation 3.17.

$$j_{syn}(\nu) = \frac{\sqrt{3}e^3 B sin(\alpha)}{m_e c^2} F\left(\frac{\nu}{\nu_c}\right) \tag{3.17}$$

where B is the magnetic field, α the pitch angle, ν_c the critical frequency which is defined as $\nu_c = \frac{3eB}{4\pi mc}\gamma^2 sin\alpha$ and is the frequency at which an electron would radiate its entire energy via synchrotron radiation, and F is a special function defined as the integral of the

modified Bessel function

$$F(x) = x \int_x^\infty K_{5/3}(\xi)d\xi \tag{3.18}$$

which can be approximated by

$$F(x) \propto \begin{cases} x^{1/3} & x \ll 1 \\ e^{-x}x^{1/2} & x \gg 1 \end{cases} \tag{3.19}$$

in the synchrotron formula $x = \frac{\nu}{\nu_c}$.

The asymptotic behaviour of F(x) function is the one that eventually defines the shape of the spectrum (Fig.3.24).
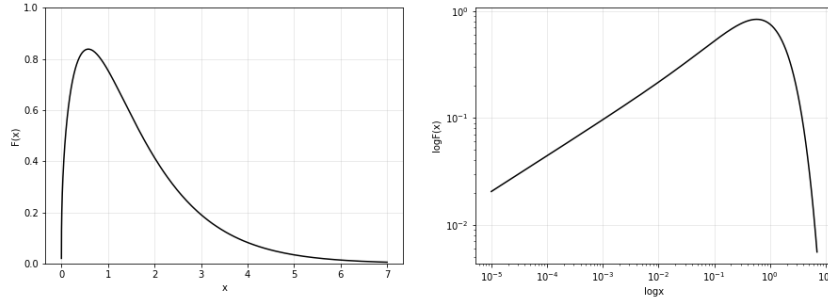
FIGURE 3.24: *Left*: how the special function F depends on parameter x, *Right*: the shape of the spectrum that a single electron produces (in logarithmic scale)

But in nature the electrons hold a range of energies. The distribution of electrons is supposed to be a power-law with the slope being an input parameter

$$\frac{dN_e}{dE} = k_e E^{-p}$$

where k_e is a normalization farctor.

In order to calculate the spectrum generated by a distribution of electrons with different energies one needs to integrate the emissivity of a single electron (eq. 3.17) over the

electron energies.

$$I_{syn}^{pl}(\nu) = \int_{E_{min}}^{E_{max}} dE N_e(E) j_{syn}(\nu) \Rightarrow I_{syn}^{pl}(\nu) \propto \begin{cases} \nu^{1/3} & \nu \ll \nu_c \\ \nu^{-\frac{p-1}{2}} & \text{intermediate frequencies} \\ \nu^{1/2} e^{-\nu/\nu_c} & \nu \gg \nu_c \end{cases}$$

(3.20)

So the produced spectrum is the sum of the peaks of each electron's spectrum, as shown in Fig. 3.25
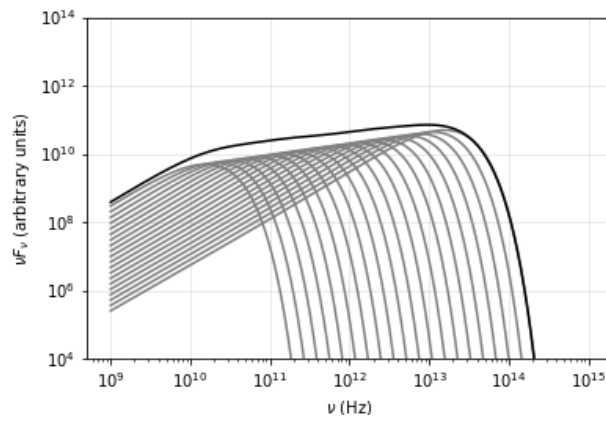
FIGURE 3.25: The synchrotron spectrum of a distribution of electrons

Chapter 4

Fitting statistics

SED-fitting is the procedure followed in order to fit a model to a set of data. The model is constructed by all the components referred in chapter 3 and the data are the observational data obtained by both online catalogues (NED, Vizier) and ALMA archive. The statistical method used has a significant role in the accuracy of the fitting and eventually the physical parameters obtained. In this chapter two of the most used test of goodness of fit are going to be presented and compared to finally explain which one of them is optimal to use.

4.1 Reduced chi-squared statistic

Assume that (x_i, y_i, σ_i) are the data, with x_i, y_i being the coordinates of each data point and σ_i its error and that they follow a Gaussian distribution with mean value the value of each point (y_i) and standard deviation its error. Additionally assuming that the function $f(x_i, \theta_i)$ represents the model we aim to fit to our points, θ_i which are the model. We can think of the model as a parameterized description of a statistical procedure that could reasonably have generated our data set. So we reverse the question and given the model we check whether and how possible it is to generate the observed data. The chi-square quantity is defined as

$$\chi^2 = \sum_{i=1}^{n} \frac{[y_i - f(x_i, \theta_i)]^2}{\sigma_i^2} \qquad (4.1)$$

and the best model is the one that minimizes the chi-square quantity (eq. 4.1).

However, the leastsquare method introduces degeneracies, which means that two different parameters of the model could give the same final curve. But the chi-square method cannot distinguish between those two. In problems of best fit there is not a correct answer. What we are aiming for is the curve with the highest possibility among the other ones. This can be achieved and visualised by using the Bayesian method.

The same thing can be described using the likelihood notation. The likelihood function is measurement of the goodness of fit of a statistical model to a sample of data for given values of the unknown parameters. For the same data and model as described above, its definition is

$$\mathcal{L}(data|model) = \prod_{i=1}^{n} \mathcal{L}(data_i|model_i) \Rightarrow \tag{4.2}$$

$$\mathcal{L}(data|model) \propto exp\left[-\sum_{i=1}^{n} \frac{(data_i - model_i)^2}{2\sigma_i^2}\right] \Rightarrow \tag{4.3}$$

$$\mathcal{L}(data|model) \propto exp(-\chi^2) \tag{4.4}$$

So in this case we seek for the model that maximizes the total likelihood. As shown in equation 4.4 this is equal to searching for the model that minimizes the chi-square (Hogg et al., 2010).

4.2 Bayesian inference

Before getting into using Bayesian statistics to fit a model to given data points we need to refer to the two basic rules that Bayesian theory derives from. Suppose that M and D stand for two propositions that are true, while $\bar{M}$ stand for the proposition M not being true. Then the two basic rules are

$$P(M, I) + P(\bar{M}, I) = 1 \tag{4.5}$$

$$P(M, D, I) = P(M|D, I)P(D, I) = P(D|M, I)P(M, I) \tag{4.6}$$

Equation 4.5 is the sum rule and states that the sum of the probability of a proposition being true plus the probability of it being untrue is one. Equation 4.6 is the product rule and states that the probability of two propositions being true is equal to the conditional

possibility of one being true given the other is true. I denotes relevant background information that is used to construct the probabilities and it can be ignored.

So from eq. 4.6 we can obtain the Bayes' theorem, assuming M is the model and D the data

$$P(M|D) = \frac{P(D|M)P(M)}{P(D)} \qquad (4.7)$$

$P(M|D)$ is called posterior probability and expresses the probability of a model M given the data D. $P(D|M)$ is the likelihood that the data be observed given the model M. $P(M)$ is called prior and contains prior knowledge of M model being true. Finally, $P(D)$ is called evidence and serves the purpose of normalizing the posterior possibility to unity but in the calculations it can be ignored.

In order to use this method for fitting a model one needs to compute the likelihood and implement the appropriate priors. Priors are one of the most important ingredients of the Bayesian framework and selecting the right ones is decisive for each problem. Priors can be classified into two categories, the uninformative and informative ones. The former are used in the case we have very little knowledge about the parameters of our model and they do not have adequate restricting power. On the other hand, informative priors confine the useful parameter space, since we use them in the case of having information for the model parameters from previous analysis for example.

When using more than one model to fit your dataset it is needed to pick the "best" model. In order to do this we need to compare all the models with each other. Let's assume we have two models M_1 and M_2. Calculating the ratio of their posteriors, yields the so called *Bayes factor* (eq. 4.9).

$$\left. \begin{array}{l} P(M_2|D) = \dfrac{P(D|M_2)P(M_2)}{P(D)} \\[2ex] P(M_1|D) = \dfrac{P(D|M_1)P(M_1)}{P(D)} \end{array} \right\} \Rightarrow \frac{P(M_2|D)}{P(M_1|D)} = \frac{P(D|M_2)P(M_2)}{P(D|M_1)P(M_1)} \qquad (4.8)$$

The main information through which two models can be compared is the likelihood of each model ($P(D|M_i)$). More specifically, in our case the prior distributions are the same so, the Bayes factor is defined as

$$B_{21} = \frac{P(M_2|D)}{P(M_1|D)} = \frac{P(D|M_2)}{P(D|M_1)} \qquad (4.9)$$

The Bayes factor can show what is the most preferable model, depending on its values. If it is bigger than one then the M_2 model is the most suitable, otherwise the M_1 model is the one. Nonetheless, calculating the Bayes factor can be computationally challenging, that is why another approximation is used. This is the BIC factor (Bayesian Information Criterion). It is defined as

$$BIC = d[ln(n)] - 2ln(P(D|M)) \qquad (4.10)$$

where d is the number of parameters describing the model, n the number of data points and $P(D|M)$ the possibility of observing the data given the model M, or in other words the likelihood. The lower the BIC value the better the model (Sharma, 2017).

After having structured the problem in the Bayesian framework one needs to follow a method to estimate the probability density function (PDF) of the parameters given the data. The PDF represents the probability of a random variable existing within a particular range of values. This probability is obtained by integrating variable's PDF over that particular range. The PDF has no negative values and the integral over its full range is 1. The most popular method used is called Markov Chain Monte Carlo (MCMC) (Goodman, Weare, 2010).This method uses a Markov chain to sample a PDF and eventually to create a sample distributed with the preferable distribution. After that it is possible to compute expectation values and integrals of the parameters embedded in the model.

Python provides us with a package with all the above information and procedures about Bayesian inference implemented. It is called "emcee" and it is an MIT licensed pure-Python implementation of Goodman, Weare (2010).

4.3   Chi-square vs Bayesian method

In this section I present an example fit that shows the different results of the two methods described above. Specifically, I perform a fit in the frequency range $10^{10} - 10^{15}$ Hz of the SED of the galaxy HE1353 using both methods. In order to perform the fit I use four components, stars, dust, AGN torus and BBB.

Fig. 4.1 shows the resulting fit as it was obtained using the least chi-square method. The curve seems to adequately approach almost all the data points so one would say that it
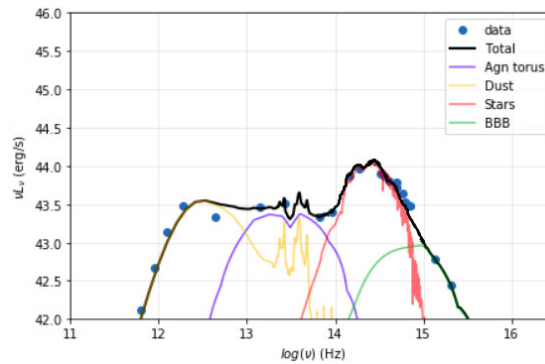
FIGURE 4.1: The best fit as was obtained by the least chi-square method

is reliable to use this method. However, when following the least chi-square method it is not feasible to test whether there are degeneracies and whether this result is the only acceptable one. Since we initially know that the SED-fitting is a degenerate problem automatically we know that we need a better method that will help us visualize our results.

What is different in the Bayesian method is that the results are given in a way that we can test whether there are groups of parameters that give the same results. The possibilities of the whole range of the parameter space are shown in the so called corner plots (Fig 4.2). In these plots we can see a histogram above each parameter of our model that represents the possibility of each value of the parameter combined with all the rest of the parameters of our model. Another important difference is that in the Bayesian method we have the advantage of the priors. As it was mentioned above, the priors are functions that we can use when having some prior knowledge about the galaxy we are studying. In this way we can brake some of the degeneracies that arise in this kind of problems.

In this case we can see that the majority of the parameters are clearly selected by the fitter with insignificant variance, since the PDF histograms appear to be delta function-like. The resulting Bayesian fit is shown in Fig. 4.3. So there are cases where the difference between the least chi-square and Bayesian method are interchangeable.

However there are more complicated cases where we can distinguish the difference between the results of the two methods. A case like this is the following example which concerns the existing degeneracy between the BBB and stellar emission. As it was mentioned in section 3.4.1 the BBB emission peaks at optical wavelengths. Young and massive stars,
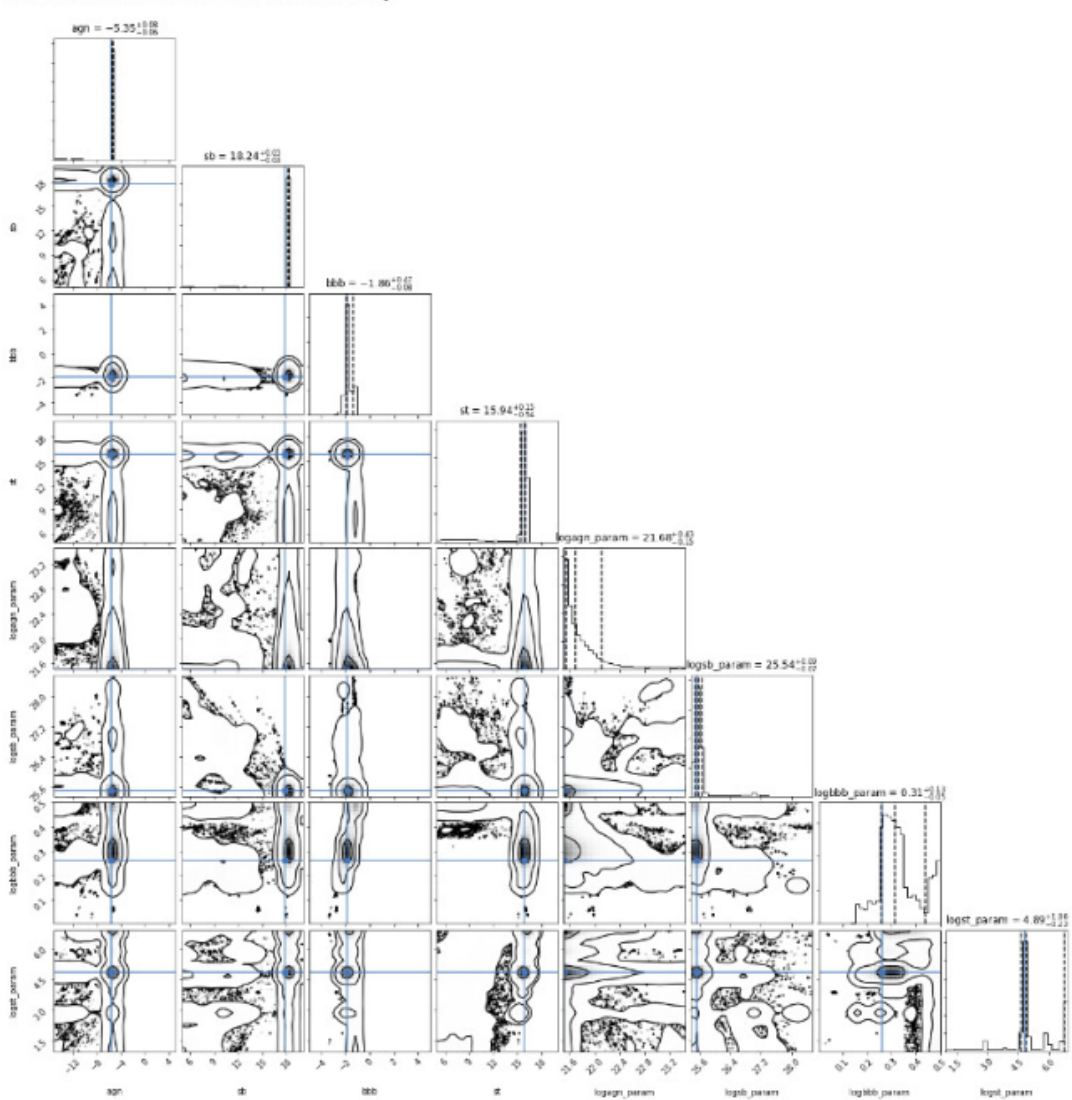
FIGURE 4.2: Corner plots

although, radiate at the same wavelengths (sec.3.1), leading to a degeneracy between the two components.

The result of the least chi-square fit is shown in Fig. 4.4. The best fit appears to be the combination of the BBB and stellar emission.

On the other hand, by using the Bayesian method we obtain the following corner plots (Fig. 4.2). We can observe that the parameter corresponding to the stellar template normalization (second plot from the left) appears to have more than one possible values. This is where the degeneracy of the problem becomes evident. In particular, the Bayesian method can give two solutions, one where the data points can be fitted only by the stellar
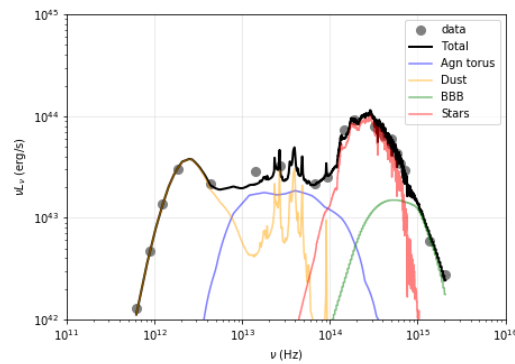
FIGURE 4.3: Best fit of the SED of the galaxy HE1353 using the Bayesian method

component (Fig. ...) and another one where the fit is managed by both BBB and stellar component.
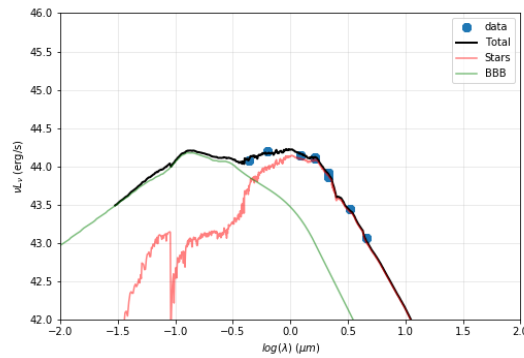
FIGURE 4.4: Least chi-square best fit

Degeneracies like the one mentioned above could break by using prior functions. For the specific example, if we knew that the galaxy under consideration is a young, type 2 AGN someone would expect to observe only young stellar emission and no BBB emission. Inserting this information in the form of a prior will give eventually the right and more physical result.

Hence, for problems like SED-fitting using Bayesian statistics is the optimal method because it manages to visualize the parameter space of our problem and also yields results that are physically accurate as long as we implement the appropriate priors.
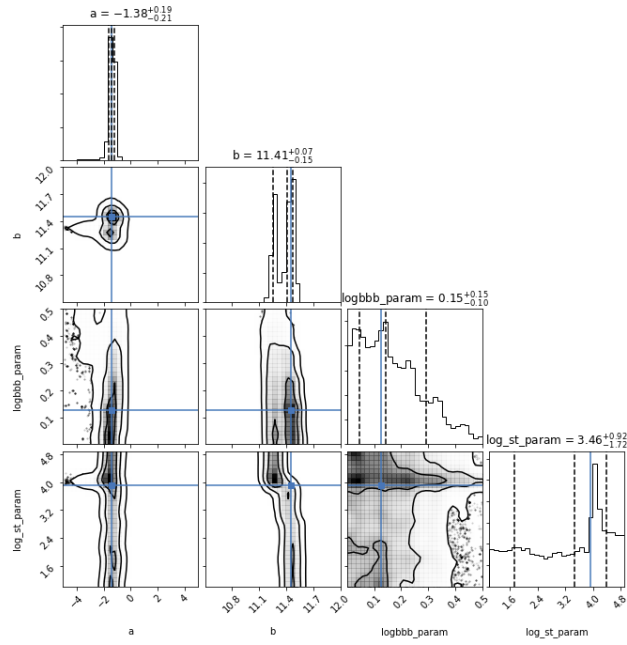
FIGURE 4.5: Corner plots. The degeneracy is apparent in this case

(A)   (B)
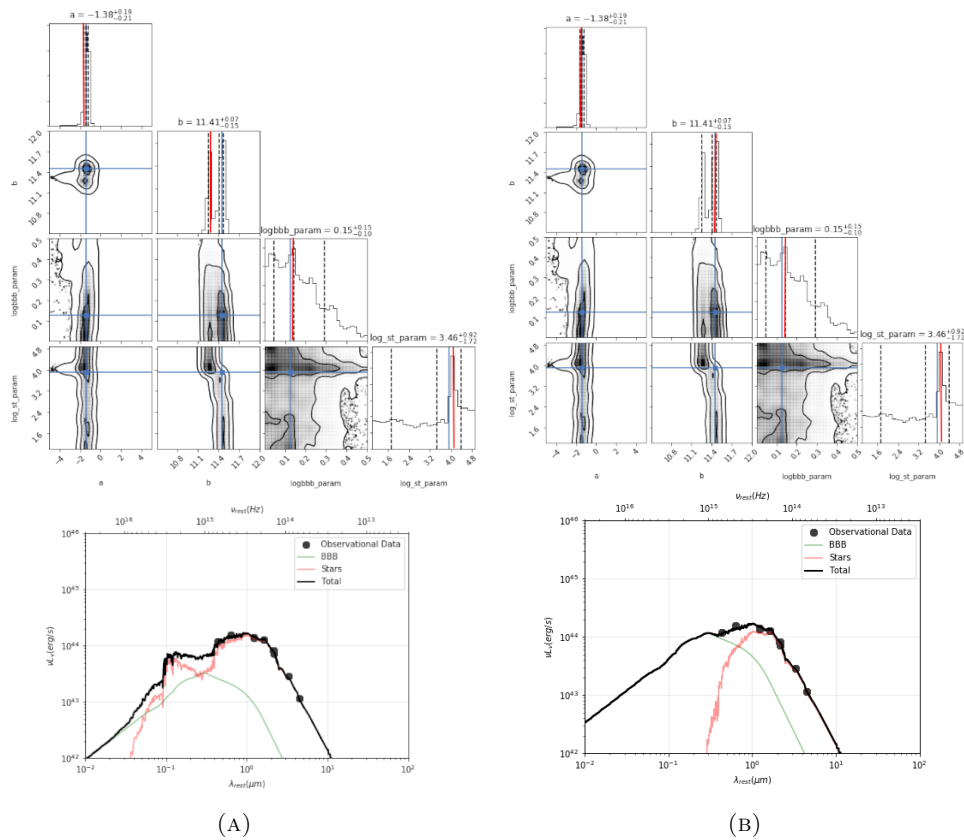
FIGURE 4.6: [A]: in the top panel we can see the values selected from the corner plot and in the bottom panel the resulting fit including only the stellar component, [B]:in the top panel we can see the values selected from the corner plot and in the bottom panel the resulting fit including both the BBB and stellar component

Chapter 5

SED fitting

In the previous chapters I explained the composition of a galactic SED, the physical processes behind each component, how they are modeled and the preferred statistical method for the SED-fitting. In the first section of this chapter I present the flow of the code that, I have developed to perform the fitting of my model to the observational data points. In the second section I explain how I obtain the physical parameters needed for the scientific interpretation from the best fit given by the code.

5.1 Code description

The code is divided into three parts. The first one is the input, where the observational data and each component's templates are inserted. The second one is the fitter, where the Bayesian code performing the fitting is developed. And the third one is the output, where the results are presented.

5.1.1 Input

In this part of the code we insert the observational data of the galaxy, which we have obtained from online catalogues and the ALMA archive, as well as the corresponding templates that are going to construct the model.

For the observational data we used the python astroquery package to mine through ALMA archive for every observation made for each object in ARC. Mining was conducted using

the astroquery package, which searched from a list of alternative names for each object given by ARC. For the mining through the ALMA archive the Alma.query object function was used. For unregistered sources we searched in a radius of 2 arcsec around its registered sky coordinates (M.Papachristou PhD thesis). This resulted in the SED of each galaxy in our sample, substantially a flux-frequency plot (Fig. 5.1).
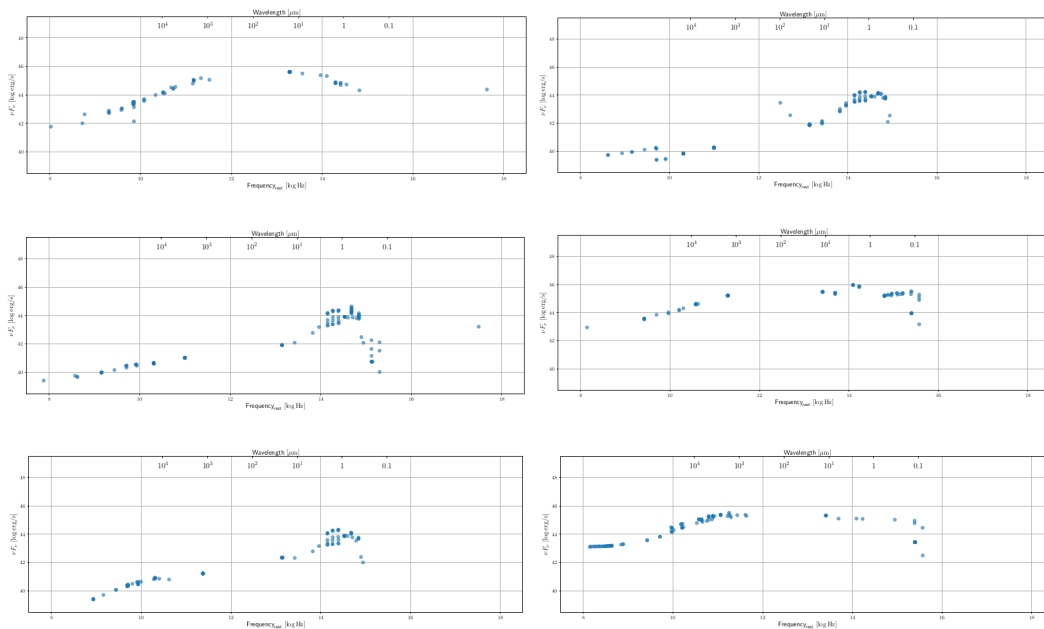
FIGURE 5.1: Some of the SEDs of the galaxies in our sample as they were downloaded after the mining procedure

However, the procedure followed to gather all the data points is an automatic one, so there are cases where the data points need to be excluded. The most important and usual reason that this needs to be done is aperture problems. Some galaxies are too extended to fit in the aperture of the telescope, hence the observed flux is lower than the real one. That is why in some SEDs in Figure 5.1 we can see that for a specific frequency there are more than one data points, since different telescopes use different apertures.

To correct this effect the first step is to calculate the aperture that would be enough for each galaxy to be observed. This demands the calculation of the angle θ (Fig. 5.2) within which an observer can observe the galaxy. Because of the expansion of the universe, the proper transverse distance corresponding to a specific opening angle depends on the redshift. So, in order to estimate the opening angle θ, that corresponds to the assumed galaxy's diameter (d), I use the scaling factor (arcmin/kpc) (Padmanabhan, 2017) that

transforms the distance to angle depending on the redshift of the observed source (eq. 5.1). For my calculations I assume that the galaxy's diameter is 30kpc.
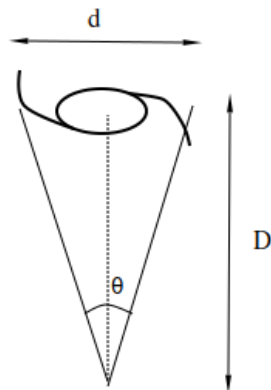
FIGURE 5.2: Scheme of the opening angle θ of an observed galaxy with diameter d, at luminosity distance D.

$$\theta = \left(\frac{kpc}{arcmin} \right)\Bigg|_{z} d \tag{5.1}$$

Since we have calculated the aperture of the galaxy, under consideration, the next step is to check each point in the galactic SED and read the report of the telescope that published the observation to make sure that the used aperture was close to the right one. A smaller aperture is not acceptable as it misses flux but a much bigger one is not desirable either, since in such a case there is high risk of including light coming from the vicinity of the galaxy-target. In Figure 5.3 we see the SED of the same galaxy before and after examining each data point.

The other input information is the templates representing each component. As it was mentioned in chapter 3 the only way to model each component of the galactic SED is to use templates that are the results of dedicated studies in the literature. This does not apply to the case of synchrotron radiation since there is a mathematical formula to describe this physical process. The "emcee" python package demands the input parameters to be continuous and not discrete, as the number of the templates are. So, we need to transform the discrete number of templates to analytic representation of them. Interpolation between the existing templates takes care of this.
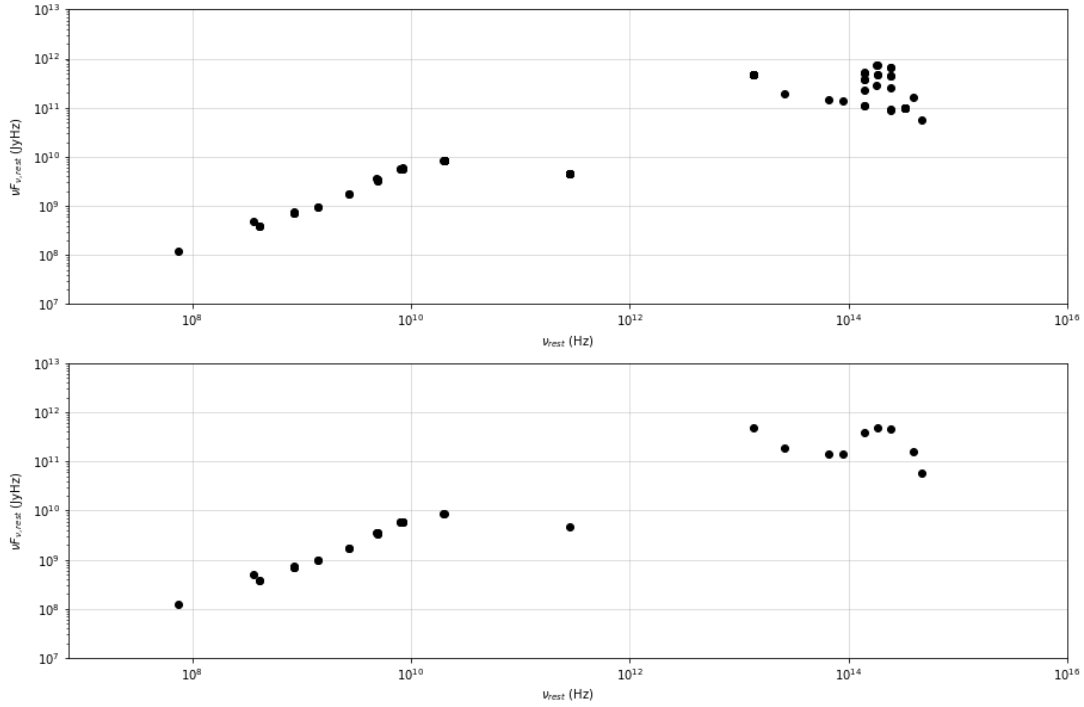
FIGURE 5.3: *top panel*: SED of galaxy J1356-3421 as it appears right after the mining, *bottom panel*: SED of the galaxy J1356-3421 after examining each data point for aperture errors

The interpolation between the templates is two-dimensional. Each template consists of a finite number of points (λ,F) and corresponds to an indexing parameter (ind) that encapsulates a series of physical parameters. Two-dimensional interpolation means that the input is a 2D-array (λ,ind) in contras to the usual 1D interpolation. The output is a function that can give the corresponding F value depending on the input indexing value. For thorough comprehension of the interpolation procedure see the example in A.

Before starting the interpolation procedure it is important to decide what is the most appropriate interpolation method and what set of parameters are going to be used to index the existing templates. Each component of the SED is a different case, so we need to explain each one of them in detail.

The set of templates for the *stellar component* are created by using the CIGALE software (Boquien et al., 2019). In order to produce the templates there are six input parameters that need to be defined.

– t_{main}: the age of the galaxy; is defined by the redshift of the galaxy we aim to fit; values range [0, galaxy's z] Gyr

– τ_{main}: the e-folding time of the main star formation episode; values range [0, 0.6] in units of t_{main} (values suggested by software's author Boquien et al. 2019)

– t_{burst}: the age (look back time) of the second star formation episode (if existing); values range [0, 0.25] in units of t_{main} (values suggested by software's author Boquien et al. 2019)

– τ_{burst}: the e-folding time of the second star formation episode; values range [0, 20] in units of t_{burst} (values suggested by software's author Boquien et al. 2019)

– f: the ratio of mass that is created by the second star formation episode; values range [0, 1]

– E(B-V): the reddening that defines the amount of attenuation that the stellar light has undergone; values range [0,0.9] (typical values from other works Vacca, Torres-Dodgen 1990; Pandey et al. 2003)

The parameter t_{main} is set to a constant value since it is defined by the galaxy's redshift. For the rest of the parameters, $t_{burst}, \tau_{burst}, f, \tau_{main}, (B - V)$, I insert a grid of values. Even though there are strong degeneracies between these parameters, which means that the resulting templates have similar forms, I set a rich grid of values to all the parameters in order to get all physically plausible results.

Since there are more than one parameters defining each stellar template the indexing parameters cannot be physical. Contrarily, they are selected in a way that they simply enumerate the existing templates. They are put in ascending order, starting from 1 and reaching up to the number of the templates. But each index corresponds to a specific combination of values of the parameters $t_{burst}, \tau_{burst}, f, \tau_{main}, (B - V)$ that have constructed the template. Some of the index values are shown in Table 5.1, in order for the reader to understand how the indexing is constructed. Additionally, the most appropriate interpolation method for the stellar templates is the "nearest", since they are defined by more than one physical parameters which we cannot be sure whether they are linearly correlated with each other. So, by using the "nearest" interpolation method the fitter picks a pre-existing template.

The set of *galactic dust templates* are the ones presented in Dale et al. (2014) (see sec. 3.2). In this case the indexing parameters correspond to physical parameters. More specifically,

TABLE 5.1: How the interpolating parameters for the stellar templates are constructed

τ_{main}	t_{burst}	τ_{burst}	f	E(B-V)	Interpolation parameter
10	500	50	0.001	0.0	1
10	500	50	0.001	0.1	2
10	500	50	0.001	0.2	3
...	...	...	...	...	...
10	500	50	0.001	0.9	19
100	1000	50	0.01	0.0	40
100	1000	50	0.01	0.1	41
100	1000	50	0.01	0.2	42
...	...	...	...	...	...
100	1000	50	0.01	0.9	49

each index corresponds to the integral of each template. The integral of a dust template refers to the total IR luminosity. So, since only one physical parameter determines the dust templates it is optimal to use the linear interpolation method. The interpolation parameters are presented in Table 5.2.

TABLE 5.2: How the interpolating parameters for the galactic dust templates are constructed

L_{IR} (erg/s)	Interpolation parameter
$10^{25.356}$	25.356
$10^{25.756}$	25.756
$10^{26.146}$	26.146
...	...
$10^{28.512}$	28.512

For the *BBB component*, as mentioned in sec. 3.4.1, I use the templates developed by Hubeny et al. (2000). The parameter used to interpolate between the existing templates is the reddening factor E(B-V). The selected grid of values is [0, 0.9] in a step of 0.1. There is only one physical parameter defining the templates so the selected interpolation method is "linear". The interpolation parameters are shown in Table 5.3.

TABLE 5.3: How the interpolating parameters for the BBB templates are constructed

$E(B-V)$	Interpolation parameter
0	0
0.1	0.1
...	...
0.9	0.9

For the *AGN torus component* I use the CAT3D model templates (see sec. 3.4.2). The input parameters that construct the templates are six.

– power-law index a: defines the radial distribution of dust clouds along the line of sight ($N_o \propto r^a$) - [0 or 1]

– N_o: number of clouds along the line of sight - [5 or 10]

– θ_o: the half-covering angle of the torus - [30°,60°]

– τ_ν: optical depth of each cloud - [50]

– R_{out}: the outer radius of the torus - [$450r_{sub}$]

– i: inclination - [$0^o, 15^o, 30^o, 45^o, 60^o, 75^o, 90^o$]

The parameters, τ_ν, R_{cl}, and R_{out} are set to a constant value in the model, by default. Specifically, $\tau_\nu = 50$, $R_{cl} = 0.035r_{sub}r$, and $R_{out} = 450r_{sub}$ (cloud and outer radius are in units of sublimation radius, which I set at the part of conversion from model flux to real flux - sec. 3.4.2). For the rest of the parameters I set a grid of values, according to the ranges allowed by the model. These four parameters are the ones that should be included in the construction of the interpolation parameters (see Table 5.4), in similar way as in stellar templates.

TABLE 5.4: How the interpolating parameters for the AGN torus templates are constructed

i	α	N_o	θ_o	Interpolation parameter
0°	0	5	30°	1
0°	1	5	30°	2
...	...	...	...	...
15°	0	5	30°	9
15°	1	5	30°	10
...	...	...	...	...
30°	0	10	60°	20
30°	1	10	60°	21
...	...	...	...	...
90°	1	10	30°	55
90°	1	10	60°	56

The last part of the code that needs to be filled is the model (eq. 5.2), so the fitter knows what is the model we aim to fit to the inserted observational data. This is where we include all the components that construct the galactic SED, either they are described by a mathematical formula or a set of templates. The SED model is defined as

$$Model = 10^{a_{st}}T_{st} + 10^{a_d}T_d + 10^{a_{bbb}}T_{bbb} + 10^{a_{tor}}T_{tor} + 10^{a_{syn}}\nu^{-\alpha}e^{-\frac{\nu}{\nu_c}} \qquad (5.2)$$

where

- T_{st}: the best stellar template out of the inserted set of templates

- a_{st}: the normalization parameter for the stellar template

- T_d: the best dust template out of the inserted set of templates

- a_d: the normalization parameter for the dust template

- T_{bbb}: the best bbb template out of the inserted set of templates

- a_{bbb}: the normalization parameter for the bbb template

- T_{tor}: the best AGN torus template out of the inserted set of templates

- a_{tor}: the normalization parameter for the AGN torus template

- $\nu^{-\alpha} e^{-\frac{\nu}{\nu_c}}$: synchrotron formula

5.1.2 Fitter

After having defined the input section of the code the next part that needs to be developed is the fitter which, as it was mention in chapter 4, follows a Bayesian inference. The goal of a Bayesian fitter is to calculate the posterior probability, which can be managed after calculating the likelihood and the prior (see eq. 4.7).

In the code there is a function defined to calculate the likelihood. Since we have prescribed the model and have inserted the data, this function calculates the product of likelihoods of each data point (eq. 4.4).

Moreover, in the code there is the "prior" function. This is the most important part of the code because this is where it is differentiated from the others (e.g. AGNfitter, Rivera et al. 2016). In this section is where we can include any kind of prior function, depending on the prior knowledge we have for each galaxy. We use the mass function as a prior distribution for all the galaxies we fit, and in particular its higher mass end. We, particularly, implement the mass function (Ilbert et al., 2013) and its evolution with respect to the redshift of the galaxy we aim to fit. In this way the probability of each stellar template, which eventually is going to yield the stellar mass of the galaxy (see

sec. 5.2.2), is modified accordingly. Before inserting the mass functions we cut them at $M = 10^{10} M_\odot$, since all the galaxies in our sample are more massive than this threshold. The mass function for each redshift bin is shown in Fig. 5.4, where we can see that the y-axis units are number of galaxies per mass. The prior functions inserted in the code need to be probability distributions, so we convert the number of sources per mass to probability. We manage it by dividing each mass function bin by the integral of the mass function. In this way the integral of the new distribution adds to unity (Fig. 5.4).

(A)

(B)
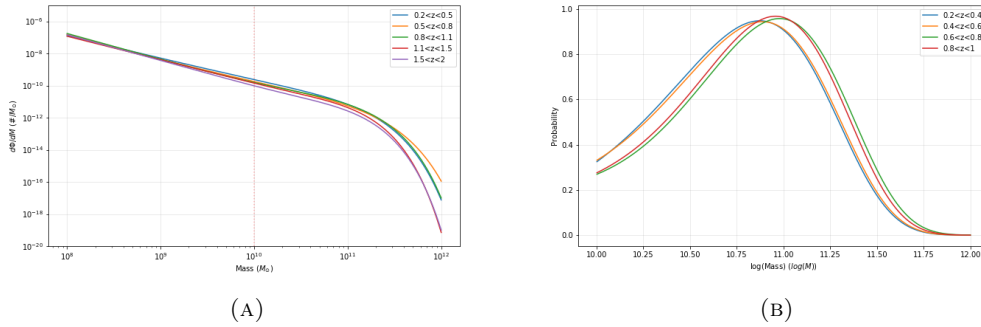
FIGURE 5.4: [A]: Mass functions for different redshift bins, [B]: Probability distribution for different redshift bins (for masses $M > 10^{10} M_\odot$) (Ilbert et al., 2013)

Except for the global prior function referred above, we can include specific prior functions for each parameter separately. The default setting is the uniform prior, which essentially is no different than the least chi-square method besides any reasonable limits. In order to take advantage of the Bayesian method we have to add a prior distribution other than the uniform, like a Gaussian, a step function, a beta or gamma distribution (Fig. 5.5). When having information for a specific parameter of the galaxy, e.g. from other studies in the literature, we can implement them in the code by using the most appropriate distribution with the right parameters.

After having defined the likelihood and prior calculator, the "emcee" package utilizes them to perform the MCMC, which was mentioned in section 4.2. Before the final run, the user needs to set the sampler. It includes the determination of the number of parameters to be fitted, the number of walkers that the MCMC sampler is going to use and the number of steps that each walker is going to make. When the sampler is ready the "emcee" function runs the input parameters and gives the results in the from of corner plots.

(A) Uniform distribution

(B) Gaussian distribution

(C) Beta distribution

(D) Gamma distribution
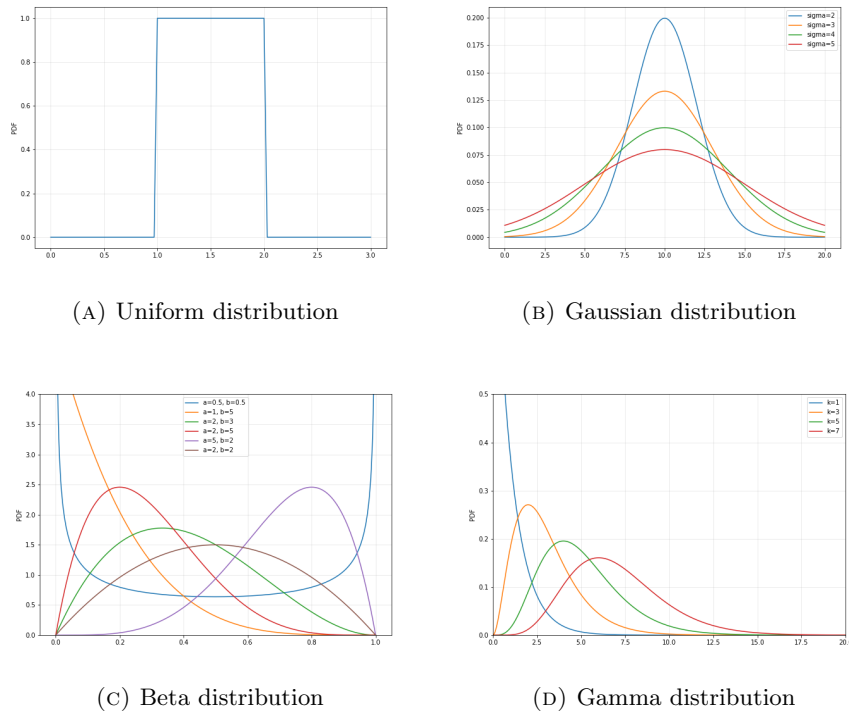
FIGURE 5.5: Different types of probability distributions

5.1.3 Output

The output of a Bayesian method is a group of corner plots, as the ones presented in section 4.3. The information presented in these plots is the PDFs of the fitting parameters, which are the posterior probabilities presented in eq. 4.7. Specifically, the histograms on the top of each column represent the PDF of each parameter (1D PDF), while the interior contour plots represent the PDF of the combination of two parameters (2D PDF). E.g. in Fig. 5.6 the red outlined contour plot shows the PDF of the combination of "st_par" and "sb_par" parameter, while the blue outlined histogram shows the PDF of "sb_par" parameter and the green outlined histogram the PDF of "st_par" parameter.

What we can also obtain from the corner plots is the median value of each parameter (the middle dashed line in each histogram) and 16th and 84th percentiles of the PDF (the other two dashed lines). I choose eventually the value of each paramter by eye, zooming as much as needed in order to find the peak of the histogram. Furthermore, I use the reported percentiles to define the error of each parameter. When the parameter shown in the corner plot is a physical one the error of the estimation is the one reported by the
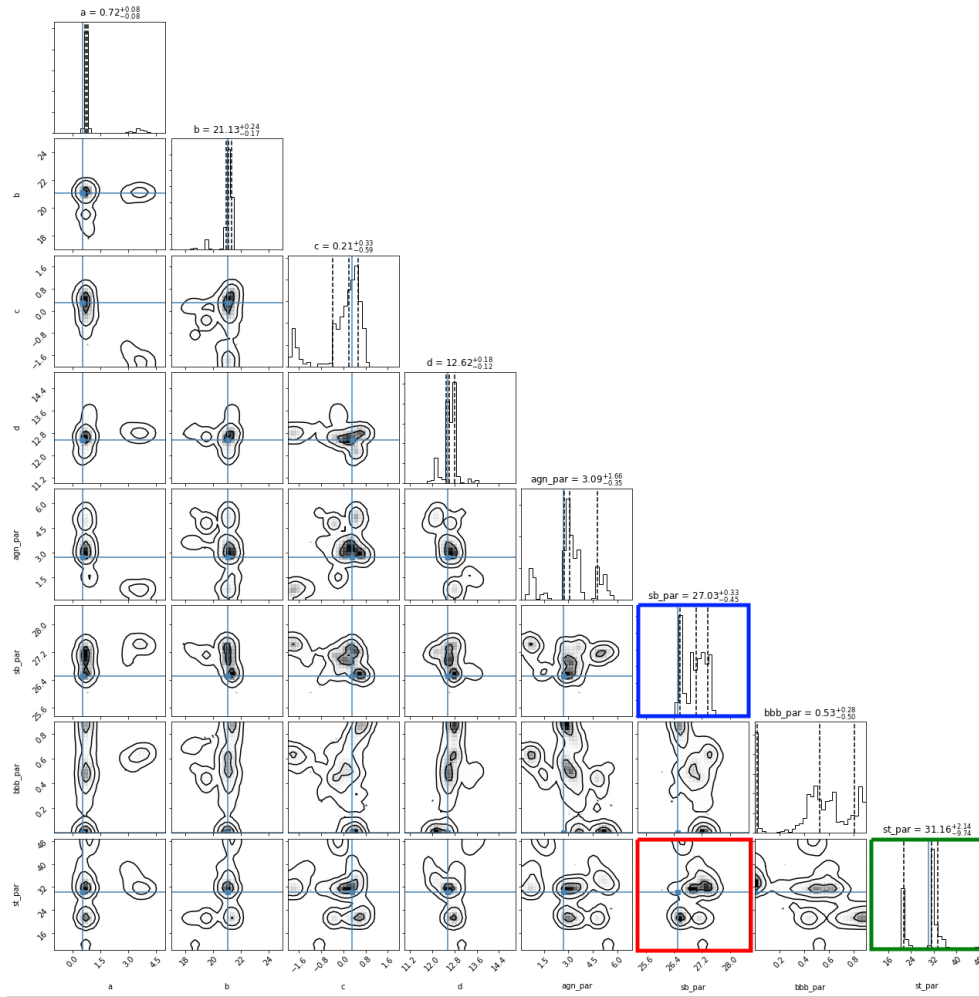
FIGURE 5.6: Example of corner plots. The histograms show the PDF of each parameter, while the contour plots show the PDF of the combination of two parameters

dashed lines. But in the case of the physical parameters that are calculated by using some of the fitting parameters (sec. 5.2), we need to calculate the propagated error.

The blue line that extends vertically and horizontally denotes the mode value, so basically the peak in the 1D PDF histogram.

5.2 Physical parameters estimation

The main reason of using SED-fitting methods is to eventually obtain as many physical quantities as possible for a galaxy and to decompose the whole SED into its individual components. Some of the physical parameters that our code allows us to yield is the IR luminosity, the stellar mass, the SFR, the jet power and the AGN luminosity. Other than

those we can also calculate the luminosity of each component, L_{bbb}, L_{dust}, L_{torus}, in order to distinguish the contribution of the host galaxy and the AGN.

5.2.1 IR Luminosity (L_{IR})

The IR luminosity information is obtained by the dust templates, since the dust emission dominates the IR wavelengths. In the NIR-MIR range there is also contribution from the AGN torus, depending on the AGN type. Type 2 AGNs are expected to have more luminous torus emission than the type 1 AGNs. But in all cases the MIR-FIR range is prominently dominated by the galactic dust.

So, the L_{IR} is calculated by integrating over the wavelengths $8 - 1000\mu m$, after subtracting the AGN torus contribution. As it was mentioned in section 5.1.1, the dust templates are indexed using the total integral of each one of them. So the T_d parameter of eq. 5.2 corresponds to the integral of the template. But because the template is multiplied with a normalization parameter (a_d) in order to fit the observational data, the L_{IR} is given by the following equation

$$L_{IR} = 10^{a_d} \cdot L_{IR}^{template} \tag{5.3}$$

Both a_d and $L_{IR}^{template}$ parameters are directly obtained by the fitter. So, as it was explained in sec. 5.1.3 the dashed lines show the errors of the fitted parameters. Hence, we obtain from the corner plots the errors δa_v and $\delta L_{IR}^{template}$. The error propagation formula (eq. 5.4) yields the IR luminosity error.

$$\delta L_{IR} = \sqrt{\left(\frac{\partial L_{IR}}{\partial(10^{a_d})}\delta(10^{a_d})\right)^2 + \left(\frac{\partial L_{IR}}{\partial L_{IR,temp}}\delta(L_{IR,temp})\right)^2} \Rightarrow$$

$$\left.\begin{array}{c} \delta L_{IR} = \sqrt{(L_{IR,temp}\delta(10^{a_d}))^2 + (10^{a_d}\delta(L_{IR,temp}))^2} \\[2mm] \delta(logx) = \dfrac{1}{x}\delta x \Rightarrow \delta a_d = \dfrac{1}{10_d^a}\delta(10^{a_d}) \end{array}\right\} \Rightarrow$$

$$\delta L_{IR} = \sqrt{(L_{IR,temp}10^{a_d}\delta a_d)^2 + (10^{a_d}\delta(L_{IR,temp}))^2} \tag{5.4}$$

5.2.2 Stellar mass (M_*)

Another physical quantity that can be obtained is the stellar mass of the galaxy. In order to calculate it we need to know the stellar mass of each SSP included in the galaxy and the

total amount of SSPs. The first piece of information is embedded in each stellar template. We mentioned in sec. 3.1 that a stellar template is structured after adding a set of SSPs and SFH. The selected SFH defines the mass-to-light ratio, which is calculated as shown in eq. 5.5. The stellar mass of the SSP is then estimated by multiplying the mass-to-light ratio by the luminosity of the referred template. The total amount of SSPs is a piece of information hidden in the normalization factor a_{st}, as defined in (eq. 5.2).

$$\frac{M_*}{L} = \frac{\int_0^t \Psi(t)dt}{\int_0^t L(t)(1 - T(t)dt)} \tag{5.5}$$

where $\Psi(t)$ is the SFH function and $T(t)$ is a function that defines the fraction of mass returned to the ISM.

So, having both the information of the stellar mass of each SSP and the amount of the SSPs leads to the stellar mass of the galaxy. This is expressed by equation 5.6.

$$M_* = 10^{a_{st}} \cdot M_{st}^{template} \tag{5.6}$$

For the purpose of the stellar mass error calculation we need the normalization factor error and the stellar mass of the template error. The former is obtained from the corner plot, while the latter is indirectly calculated. The parameter in the corner plot corresponding to the stellar template is a structured parameter, for indexing purposes, and not a physical one. That is why the calculation of the error is managed as explained in the following example.

Assume that the indexing for the stellar templates is 1,2,3,...,10 and the fitter gives the value 5 with error ± 1. Template 5 corresponds to stellar mass 0.6, while template 4 and 6 correspond to stellar mass $0.55 M_\odot$ and $0.65 M_\odot$ respectively. So, the error in the stellar mass of the template is $\delta M_{st}^{temp} = \pm 0.05 M_\odot$.

The calculation of the galactic stellar mass error is given by equation 5.7.

$$\delta M_* = \sqrt{\left(\frac{\partial M_*}{\partial a_{st}}\delta a_d\right)^2 + \left(\frac{\partial M_*}{\partial (M_{st}^{temp})}\delta(M_{st}^{temp})\right)^2} \Rightarrow$$

$$\delta M_* = \sqrt{\left(M_{st}^{temp}10^{a_{st}}\delta a_{st}\right)^2 + \left(10^{a_{st}}\delta(M_{st}^{temp})\right)^2} \tag{5.7}$$

After having obtained the stellar mass of a galaxy and assuming that the mass of the gas that is affected is the 1/10 of the stellar mass of the galaxy, one can calculate the binding energy at a specific distance. The mathematical formula is given by equation 5.8 and refers to the energy the gas should gain in order to escape from a distance R. There is a minus sign because we need to add energy to an object to unbind it.

$$U_{bind} = -(cosnt.)\frac{G(M_* M_{gas})}{R} = -(cosnt.)\frac{G \cdot 0.1 M_*^2}{R} \tag{5.8}$$

The error appears because of the error in the stellar mass calculation. So the error propagation formula yields the error of the binding energy calculation, as is shown in equation 5.9.

$$\delta U_{bind} = \sqrt{\left(\frac{\partial U_{bind}}{\partial M_*}\delta M_*\right)^2} = \frac{\partial U_{bind}}{\partial M_*}\delta M_* \Rightarrow$$

$$\delta U_{bind} = 0.2(cosnt.)\frac{G M_*}{R}\delta M_* \tag{5.9}$$

5.2.3 Star Formation Rate (SFR)

The next important quantity that can be obtained by using the fitter's results is SFR. There are several studies dedicated to the discovery of the optimal tracer of SFR (Kennicutt, 1998; Calzetti et al., 2007; Madau, Dickinson, 2014). In this work we use the correlation relation derived by Murphy et al. (2011).

In order to calculate the SFR of a galaxy we need to know the amount of young stars, so that we can have an estimation of the mass created per unit time. The best indicator of young stars is the UV part of the galactic SED, since the young massive stars radiate in the UV-optical band, as referred in section 3.1. However, the UV starlight gets attenuated by the galactic dust which re-radiates the absorbed light. So, we can get a more accurate estimation of the SFR if we also take into account the IR part of the galactic SED. Warm dust, which peaks in the MIR, encloses the most important information about SFR that should be included, while cold dust which peaks in the FIR is reported as negligible. That is because the cold dust is mainly heated by older stellar population, hence it delivers no information about the SFR. So, the proposed correlation formula by Murphy et al. (2011)

adds the UV and IR contribution up (eq. 5.12).

$$\left(\frac{SFR_{IR}}{M_\odot yr^{-1}}\right) = 3.88 \cdot 10^{-44} \left(\frac{L_{IR}}{erg s^{-1}}\right) \tag{5.10}$$

$$\left(\frac{SFR_{FUV}}{M_\odot yr^{-1}}\right) = 4.42 \cdot 10^{-44} \left(\frac{L_{FUV}}{erg s^{-1}}\right) \tag{5.11}$$

$$SFR_{tot} = SFR_{IR} + SFR_{FUV} \Rightarrow$$

$$\left(\frac{SFR_{tot}}{M_\odot yr^{-1}}\right) = 4.42 \cdot 10^{-44} \left(\frac{0.88 L_{IR} + L_{FUV}}{erg s^{-1}}\right) \tag{5.12}$$

where L_{FUV} is the integral of luminosity over 0.14-0.17 μm wavelengths and L_{IR} is the integral of luminosity over 8-1000 μm wavelengths. Note that for the calculation of the L_{IR} we integrate only over the dust template, excluding in this way any AGN torus contribution.

The error in this physical quantity emerges partially from the error in L_{IR}, which in turn comes from the error in the dust template selection by the fitter and the error in L_{FUV} which is propagated by the stellar template selection. The formula for the SFR error calculation is given by equation 5.13.

$$\delta(SFR) = \sqrt{\left(\frac{\partial(SFR)}{\partial L_{FUV}}\delta L_{FUV}\right)^2 + \left(\frac{\partial(SFR)}{\partial L_{IR}}\delta L_{IR}\right)^2} \Rightarrow$$

$$\delta(SFR) = 4.42 \cdot 10^{-44} \sqrt{(\delta L_{FUV})^2 + (0.88\delta L_{IR})^2} \tag{5.13}$$

5.2.4   Jet power (P_{jet})

The galaxies included in our sample are radio galaxies hosting a radio jet. So, it is of great significance for the scientific interpretation of this work to estimate the jet power. I use two methods to calculate the jet power, so that I can compare and check the viability of the resulting values.

The first one is integrating over the radio frequencies. In sec.3.3 I referred to the contribution of the starburst regions to the radio frequencies, due to synchrotron and bremsstrahlung

radiation. So, I simultaneously subtract the starburst contribution and fit the radio frequencies. In this way I can get only the contribution of the radio jet. After having done so, I integrate over the radio luminosity. The obtained value is considered to be the lower possible value of the radio jet. That is because only the radio band is taken into consideration.However, the radio jet's electrons could radiate to other frequencies except for the radio band (X-rays, gamma rays) while not all relativistic electrons radiate in order to be observed.

The second method is using the formula derived by Punsly (2005). According to this work X-ray observations from the lobes' hot spots, which were attributed to inverse Compton,and the surrounding extragalactic material led to a more accurate calculation of the particle energy in the lobe and eventually the energy transported by the jet. The realization that the material in the lobe is far from the equipartition led to the construction of a more realistic formula than the one presented in Willott et al. (1999). So the jet kinematic luminosity is calculated by the equation 5.14.

$$P_{jet} = 5.7 \cdot 10^{44}(1+z)^{\alpha+1}Z^2 F_{151} \qquad (5.14)$$

$$Z = 3.31 - 3.65 \left[(1+z)^4 - 0.203(1+z)^3 + 0.749(1+z)^2 + 0.444(1+z) + 0.205\right]^{-0.125}$$

where z is the galaxy's redshift and F_{151} is the flux at 151MHz, given in Jy in order for the formula to obtain the jet power in erg/s.

In the case of calculating the jet power using the Punsly (2005) formula, the error occurs due to the F_{151} value. This error emerges from the error in slope α and critical frequency ν_c, which are obtained by the fitter. Hence, the error propagation follows the relation shown in eq. 5.15.

$$\nu L_\nu = 10^{a_{syn}}\nu^{-\alpha}e^{-\nu/\nu_c} \Rightarrow L_\nu = 10^{a_{syn}}\nu^{-\alpha-1}e^{-\nu/\nu_c} \Rightarrow$$

$$F_\nu = \frac{1}{4\pi D^2}10^{a_{syn}}\nu^{-\alpha-1}e^{-\nu/\nu_c} \Rightarrow$$

$$\delta F_\nu = \sqrt{\left(\frac{\partial F_\nu}{\partial(10^{a_{syn}})}\delta(10^{a_{syn}})\right)^2 + \left(\frac{\partial(F_\nu)}{\partial\alpha}\delta\alpha\right)^2 + \left(\frac{\partial(F_\nu)}{\partial\nu_c}\delta\nu_c\right)^2} \Rightarrow$$

$$\delta F_\nu = \sqrt{\frac{10^{a_s}e^{-\nu/\nu_c}}{4\pi D^2}}\sqrt{\left(\frac{\nu^{-\alpha}}{\nu}\delta a_s\right)^2 + \left((-\alpha-1)\frac{\nu^{-\alpha}}{\nu^2}\delta\alpha\right)^2 + \left(\frac{\nu^{-\alpha}}{\nu}\left(-\frac{\nu}{\nu_c}\right)10^{\nu_c}\delta\nu_c\right)^2}$$
$$(5.15)$$

5.2.5   AGN luminosity (L_{AGN})

Another physical parameter estimated after obtaining the best-fit is the AGN luminosity (L_{AGN}). This one is easier and most straight forward to calculate, in comparison with the other mentioned quantities. The AGN emission constitutes of the BBB and AGN torus emission. So, before calculating the L_{AGN}, I integrate over the wavelengths of the bbb and torus template, in order to get the L_{bbb} and L_{torus} respectively. Eventually, the AGN luminosity is calculated by merely adding the BBB to torus luminosity.

$$L_{AGN} = L_{bbb} + L_{torus} \tag{5.16}$$

The error in this case comes from the two integrals, which in turn emerges from the parameters a_{bbb}, T_{bbb}, a_{torus}, T_{torus} (see eq. 5.2) corresponding to the bbb normalization factor and template as well as the torus normalization factor and template, respectively.

Chapter 6

Results

In this chapter I present the resulting SED fitting and the obtained physical parameters for three of the galaxies in our sample, PKS 1005+007, NGC 3100, and NGC 3557.

6.1   PKS 1005+007

The PKS 1005+007 galaxy is a BL Lac object at redshift z=0.0977, which eventually yields a luminosity distance of $D_L = 449 Mpc$ and age of the galaxy at 13.347 Gyr.

In Fig. 6.1 one can see the resulting SED fitting for the PKS 1005+007 galaxy. In the grey box, some of the obtained physical parameters are shown. As explained in Chapter 5, the physical parameters are obtained by following specific formulas and the corresponding errors are calculated by the error propagation. All the physical parameters calculated for the galaxy PKS 1005+007 are shown in the Table 6.1.

TABLE 6.1: Physical parameters of galaxy PKS 1005+007

L_{IR} $(L_\odot)$	L_{AGN} (erg/s)	M_* $M_\odot$	SFR $M_\odot/yr$	P_{jet} (erg/s)
$6 \cdot 10^{10}$	$3 \cdot 10^{43}$	$3 \cdot 10^{11}$	4.8 ± 0.6	$8 \cdot 10^{42}$

The binding energy is estimated using equations 5.8 and 5.9 after assuming that the gas gets unbind from the effective radius. A typical average value for the effective radius is R=15kpc. Another assumption is that the gas mass is about one order of magnitude lower than the L_{IR} value Sanders et al. (1991). The result appears in equation 6.1.
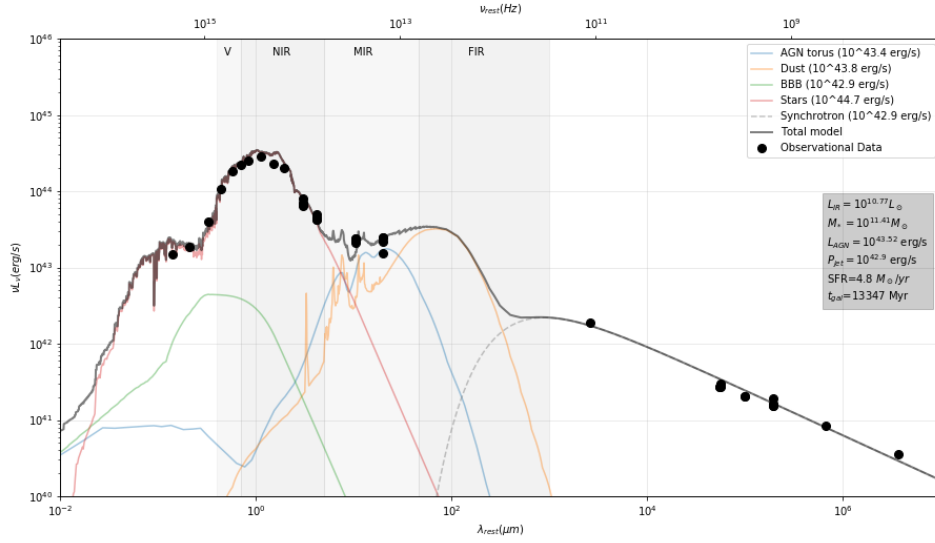
FIGURE 6.1: The resulting SED-fitting of galaxy PKS 1005+007. The different compo-
nents of the SED are denoted with different colors, as appears in the legend where one
can also see the integral of each component. The physical parameters obtained after the
best fit was managed and specific formulas were followed, are shown in the grey box on
the right.

$$U_{bind} = -(cosnt.)\frac{G \cdot M_* M_{gas}}{R} \Rightarrow$$

$$U_{bind} \simeq \frac{1.3 \cdot 10^{26}[cm^3 M_\odot^{-1} s^{-2}] 2.1 \cdot 10^{11}[M_\odot] 6 \cdot 10^9 [M_\odot]}{15 \cdot 3 \cdot 10^{21}[cm]} \Rightarrow$$

$$U_{bind} \simeq 10^{58} erg \tag{6.1}$$

The timescale during which the radio jet can expel gas away from a 15kpc radius is
obtained by dividing the binding energy by the jet power, as appears in equation 6.2.

$$t_{scale} = \frac{U_{bind}}{P_{jet}} \Rightarrow t_{scale} \simeq 4 \cdot 10^7 yrs \tag{6.2}$$

6.2   NGC 3100

NGC 3100 is classified as a LINER galaxy, at redshift z=0.0086 which means that the
galaxy exists at luminosity distance $D_L = 37$ Mpc and its calculated age is 13.35 Gyr.

In Fig. 6.2 one can see the resulting SED fitting for the NGC 3100 galaxy. In the grey box,
some of the obtained physical parameters are shown while the integral of each component
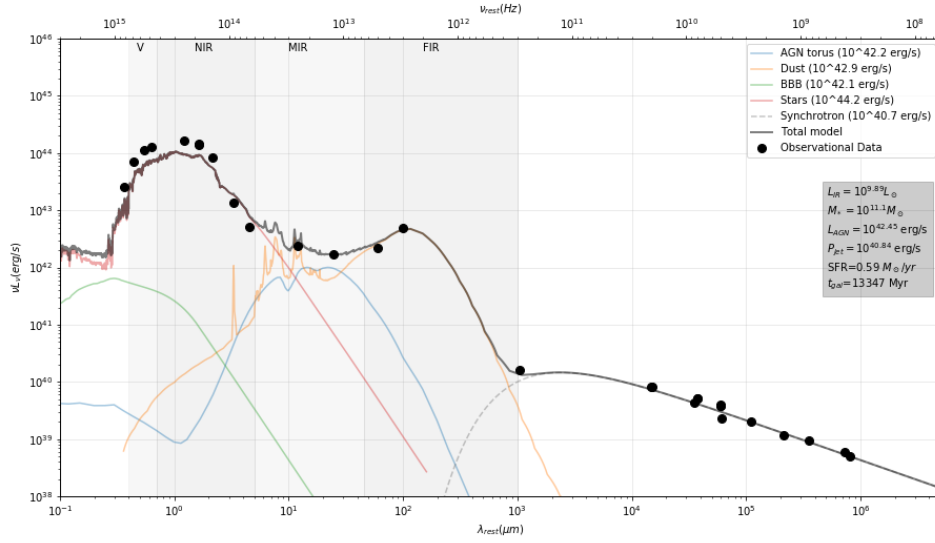
FIGURE 6.2: The resulting SED-fitting of galaxy NGC 3100. The different components of the SED are denoted with different colors, as appears in the legend where one can also see the integral of each component. The physical parameters obtained after the best fit was managed and specific formulas were followed, are shown in the grey box on the right.

appears in the legend. The obtained physical parameters of NGC 3100 are shown in the Table 6.2.

TABLE 6.2: Physical parameters of galaxy NGC 3100

L_{IR} $(L_\odot)$	L_{AGN} (erg/s)	M_* $M_\odot$	SFR $M_\odot/yr$	P_{jet} (erg/s)
$8 \cdot 10^9$	$3 \cdot 10^{42}$	$1.4 \cdot 10^{11}$	0.59 ± 0.08	$7 \cdot 10^{40}$

The binding energy of galaxy NGC 3100 is estimated as appears in equation 6.3, again assuming a distance R=15 kpc and that the gas mass is one order of magnitude lower than the L_{IR} value Sanders et al. (1991).

$$U_{bind} = -(cosnt.)\frac{G \cdot M_* M_{gas}}{R} \Rightarrow$$

$$U_{bind} \simeq 0.1 \frac{1.3 \cdot 10^{26}[cm^3 M_\odot^{-1} s^{-2}]10^{11}[M_\odot]8 \cdot 10^8 [M_\odot]}{15 \cdot 3 \cdot 10^{21}[cm]} \Rightarrow$$

$$U_{bind} \simeq 5 \cdot 10^{56} erg \tag{6.3}$$

The timescale during which the radio jet can expel gas away from a 15kpc radius is obtained by dividing the binding energy by the jet power, as appears in equation 6.4.

$$t_{scale} = \frac{U_{bind}}{P_{jet}} \Rightarrow t_{scale} \simeq 2 \cdot 10^8 yrs \tag{6.4}$$

6.3   NGC 3557

NGC 3557 is a radio galaxy at redshift z=0.01 so at luminosity distance $D_L = 43.6$ Mpc and age 13.33 Gyr. The fitted SED of this galaxy is show in Fig. 6.3.
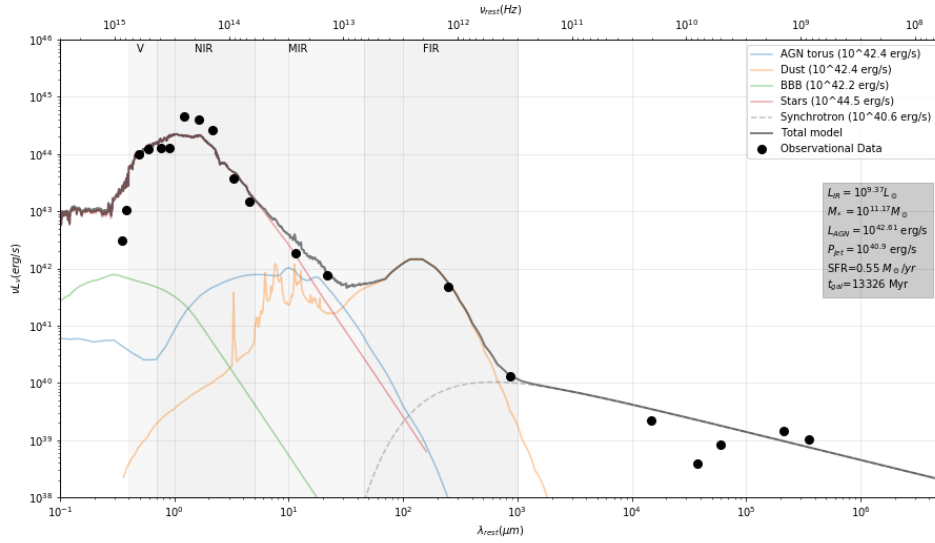
FIGURE 6.3: The resulting SED-fitting of galaxy NGC 3557. The different components of the SED are denoted with different colors, as appears in the legend where one can also see the integral of each component. The physical parameters obtained after the best fit was managed and specific formulas were followed, are shown in the grey box on the right.

The physical parameters appear in the Table 6.3.

TABLE 6.3: Physical parameters of galaxy NGC 3557

L_{IR} ($L_\odot$)	L_{AGN} (erg/s)	M_* $M_\odot$	SFR $M_\odot/yr$	P_{jet} (erg/s)
$2 \cdot 10^9$	$4 \cdot 10^{42}$	$1.5 \cdot 10^{11}$	0.5 ± 0.02	$8 \cdot 10^{40}$

The binding energy of galaxy NGC 3557 is estimated in equation 6.5, assuming a distance R=15 kpc and gas mass $M_{gas} \simeq 2 \cdot 10^8 M_\odot$ Sanders et al. (1991).

$$U_{bind} = -(cosnt.)\frac{G \cdot M_* M_{gas}}{R} \Rightarrow$$

$$U_{bind} \simeq \frac{1.3 \cdot 10^{26}[cm^3 M_\odot^{-1} s^{-2}]1.5 \cdot 10^{11}[M_\odot]2 \cdot 10^8[M_\odot]}{15 \cdot 3 \cdot 10^{21}[cm]} \Rightarrow$$

$$U_{bind} \simeq 2 \cdot 10^{56} erg \tag{6.5}$$

The timescale during which the radio jet can expel gas away from a 15kpc radius is obtained by dividing the binding energy by the jet power, as appears in equation 6.6.

$$t_{scale} = \frac{U_{bind}}{P_{jet}} \Rightarrow t_{scale} \simeq 7 \cdot 10^7 yrs \tag{6.6}$$

Chapter 7

Conclusion

The purpose of my thesis is to test whether the radio jet of a galaxy is energetically cable of unbinding part of its gas. In order to answer the imposed question, I need to calculate the radio jet power and the host galaxy's binding energy. The former is calculated directly by the SED fitting (see sec. 5.2.4), and the binding energy of the galaxy which is calculated using the obtained stellar mass (see sec. 5.2.2).

Having this information, I estimate the timescale during which the radio jet can expel gas from a minimum distance of 15 kpc. But in order to judge whether this is a credible value, I need to compare it with a physical timescale. The first timescale I should compare my results with, is the age of the galaxy and furthermore the jet duty cycle timescale. According to the literature, typical values of the jet duty cycle is of the order of 10^7 years.

The calculation of the radio jet is a lower limit for two main reasons. Firstly, the radio jet radiates except for the radio frequencies, in X-rays and gamma rays. However, we have information only about the radio band so we are missing some information. The second reason is that not all relativistic electrons radiate in order to be observable either in the radio band or the gamma rays. Since the power of the radio jet is inversely proportional to the timescale, the timescale calculation is an upper limit.

So, in PKS1005+007 since the maximum timescale needed for the radio jet to unbind the gas ($\sim 10^7$ yrs) is comparable with the jet's duty cycle, we deduce that energywise this could be a possible environment for a jet-driven outflow. Further information about this galaxy, like its gas content, will yield an even more accurate result. However, a missing but important information is the inclination of the jet with respect to the galactic disk.

Without knowing the orientation of the jet one can not be sure about how possible and efficient the radio mode can be. So studying this problem using energy arguments is a primary test needed to be made, before getting into deeper details. In addition, from the fitted SED of PKS1005+007 we can observe that there is low UV radiation leading to the presumption that there are not many young stars in this galaxy. Furthermore, the radiation of the dust seems to be low. These are typical characteristics of an elliptical galaxy, as the optical image of the galaxy can verify.

In galaxy NGC3100 the obtained timescale, under the same assumptions made above, is $\sim 10^8$ yrs. It appears to be higher than the typical jet duty cycle, but comparing it with the galaxy's age, the scenario of the jet depriving the galaxy of its gas does not seem far fetched. The fitted SED of the galaxy reveals, high enough UV radiation and low enough dust radiation to make us believe that this is a disk galaxy. This deduction can be verified by the galaxy's optical image.

Finally, in galaxy NGC3557 the time needed for the jet to expel gas is estimated $\sim 10^8$ yrs. This is a similar case as the galaxy NGC3100, where the obtained timescale is higher than the typical jet duty cycle but comparing it with the galaxy's age this timescale could be physically accepted. Finally, when it comes to the fitted SED of the galaxy, we can deduce that this is an elliptical galaxy because of the low UV and high dust radiation.

I aim to follow the method presented in my thesis, for all the 70 galaxies of our sample. So along with the results, provided by the rest of the team, on gas detections in the galaxies of the sample, I will be able to obtain statistical results. They are going to concern the percentage of radio galaxies that hold a radio jet capable of driving a molecular outflow.

Appendix A

Two-dimensional interpolation

The interpolation function used for the purposes of SED-fitting is the "RegularGridInter-polator" from Python's scipy package. This function manages interpolation on a regular grid in arbitrary dimensions and uneven spacing between the grid points. Its syntax is presented below.

scipy.interpolate.RegularGridInterpolator(points, values, method='linear', bounds_error=True, fill_value=nan)

- **points**: the points defining the regular grid in two dimensions [2d-array, axes of index and wavelength (μm)]

- **values**: the data on the regular grid in n dimensions [1d-array, flux (erg/scm^2)]

- **method**: the method of interpolation to perform [str, "linear" or "nearest"]

- **bounds_error**: If True, when interpolated values are requested outside of the domain of the input data, a ValueError is raised, while if False, then fill_value is used [True or False]

- **fill_value**: if provided, it is the value to use for points outside of the interpolation domain, while if None, values outside the domain are extrapolated [number]

This interpolator is based on the Lagrange polynomials. Lagrange is called the polynomial of degree $\leq (n-1)$, where n is the number of data points we aim to interpolate (Fig.

A.1). They are defined as appears in equation A.1.

$$P_n(x) = \sum_{j=1}^{n} P_j(x) = \sum_{j=1}^{n} \left[\prod_{k=1, k \neq j}^{n} \left(\frac{x - x_k}{x_j - x_k} \right) \right] \tag{A.1}$$

E.g. the Lagrange polynomial in the case we have three points is defined as

$$P_3(x) = y_1 \left(\frac{x - x_2}{x_1 - x_2} \cdot \frac{x - x_3}{x_1 - x_3} \right) + y_2 \left(\frac{x - x_1}{x_2 - x_1} \cdot \frac{x - x_3}{x_2 - x_3} \right) + y_3 \left(\frac{x - x_1}{x_3 - x_1} \cdot \frac{x - x_2}{x_3 - x_2} \right)$$
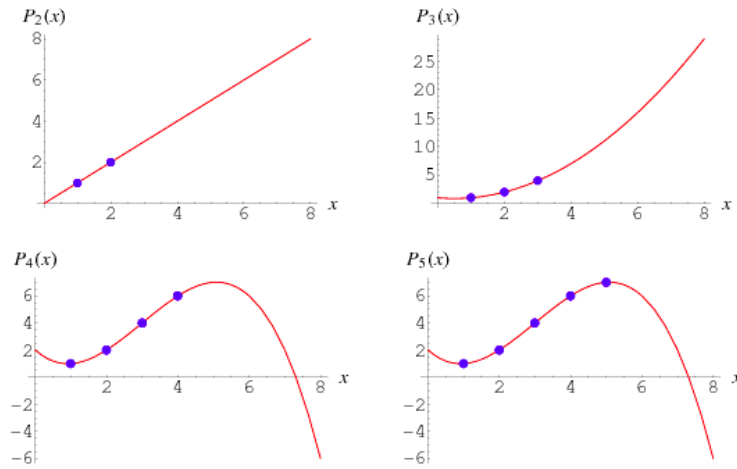
FIGURE A.1: The Lagrange polynomial for each different case of having different number of data points (source)

So, as input information I insert a grid of points, which is the concatenation of a 1D-array as the wavelength and a tuple of 1D-arrays as the index. Specifically, the grid in Fig. A.2 (A) is constructed by the 1D-array $\lambda = [0, 0.33, ..., 5.95, 6.28]$ and a tuple of 1D-arrays with same shape as λ, $index = [[-0.5, .., -0.5], ..., [0.5, .., 0.5]]$.

As it was mentioned above, after defining the 2D grid we need to insert the values of each point of the grid. The values for this example are set as $z = a_{norm} sin(x)$, where a_{norm} is a normalization factor that varies for each point. For better visualization I present the projection of the values on the x axis, in Fig. A.2 (B). Each curve corresponds to a different y coordinate value. The combination of the two planes of Fig. A.2, which is the way that the interpolator "sees" the input data, is presented in Fig. A.3.

As it is noted in this figure the interpolation of the values takes place at the direction from the lowest index value to the highest one, for constant λ at a time. The interpolation
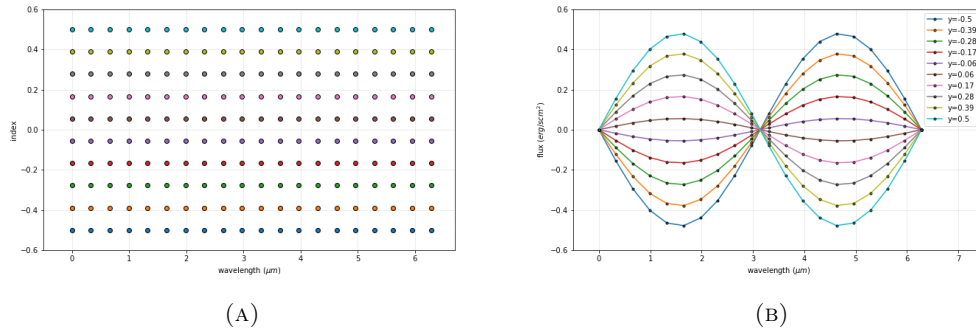
FIGURE A.2: [A]:The 2D grid constructed by inserting a 1D-array as the x coordinate and multiple 1D-array as the y coordinate, [B]:The values given at each point of the xy-grid. For better visualization I present the values with respect to the x coordinate
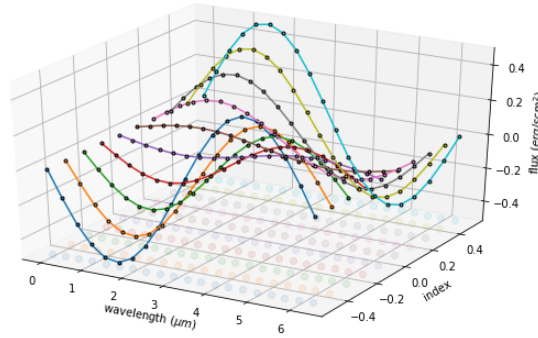
FIGURE A.3: 3D grid of points, as they appear in the interpolator

direction can be better seen in Fig. A.4.

The interpolator uses the Lagrange polynomials, along the noted direction, in order to create a function that will connect the points as accurately as possible. So, when the user requests for the curve that corresponds to a specific parameter y, the interpolator is able to generate the values in z axis that will shape the requested curve.

The quantities I use in my SED-fitting, correlate with the ones referred to the above example. More specifically, the x coordinate corresponds to the frequencies of each template, the z values the fluxes of each template and the y coordinates to the indexing parameters.

Example for comprehension
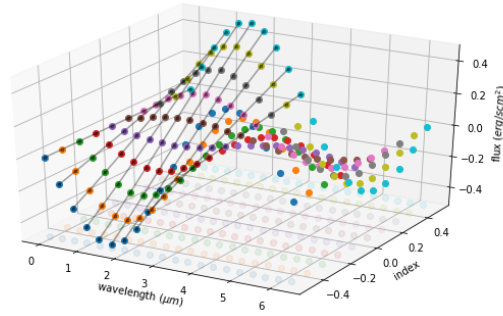
FIGURE A.4: Same image as the one in Fig. A.3 with the only difference that the interpolation direction becomes more prominent)

Assume that we have three templates, which we correspond to three parameters (1, 2, 3). There are two interpolation options, the "linear" and "nearest". The linear interpolation, when giving a parameter inside the appropriate range, e.g. 1.8, returns a template in-between the existing ones. This procedure is depicted in Fig. A.5 [A], where the existing templates are denoted with black and correspond to parameters 1 and 2, respectively and the linearly interpolated template, corresponding to the parameter 1.8 is depicted with red. The nearest interpolation, on the other hand, when giving a parameter returns the template whose parameter is closest to the given one. In Fig. A.5 [B], the given parameter is 1.8 so the nearest interpolation returns the template corresponding to param=2. This is the method used to interpolate all the existing templates of each component before adding them in the code. More details about the way the 2D interpolator works are presented in Appendix A.
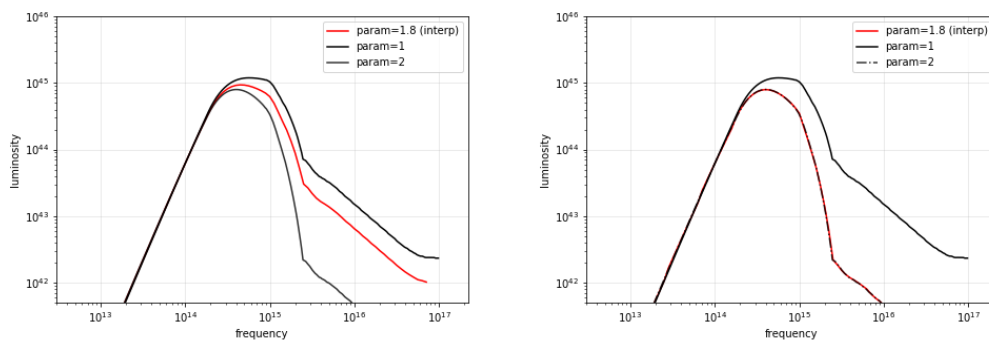
FIGURE A.5: [A]: Linear interpolation between two templates, [B]: Nearest interpolation between the same two templates

Bibliography

Aalto S., Costagliola F., Muller S., Sakamoto K., Gallagher J. S., Dasyra K., Wada K., Combes F., García-Burillo S., Kristensen L., Martín S., Werf P. van der, Evans A. S., Kotilainen J. A precessing molecular jet signaling an obscured, growing supermassive black hole in NGC1377? // A&A. VI 2016. 590. A73. arXiv: 1510.08827.

Aalto S., Garcia-Burillo S., Muller S., Winters J. M., Werf P. van der, Henkel C., Costagliola F., Neri R. Detection of HCN, HCO+ and HNC in the Mrk231 molecular outflow - Dense molecular gas in the AGN wind // A&A. I 2012a. 537. A44. arXiv: 1111.6762.

Aalto S., Muller S., Sakamoto K., Gallagher J. S., Martin S., Costagliola F. Winds of change - a molecular outflow in NGC 1377? The anatomy of an extreme FIR-excess galaxy // A&A. X 2012b. 546. A68. arXiv: 1206.4858.

Alatalo Katherine, Blitz Leo, Young Lisa M., Davis Timothy A., Bureau Martin, Lopez Laura A., Cappellari Michele, Scott Nicholas, Shapiro Kristen L., Crocker Alison F., Martin Sergio, Bois Maxime, Bournaud Frederic, Davies Roger L., Zeeuw P. T. de, Duc Pierre-Alain, Emsellem Eric, Falcon-Barosso Jesus, Khochfar Sadegh, Krajnovic Davor, Kuntschner Harald, Lablanche Pierre Yves, McDermid Richard M., Morganti Raffaella, Naab Thorsten, Oosterloo Tom, Sarzi Marc, Serra Paolo, Weijmans Anne-Marie. Discovery of an AGN-Driven Molecular Outflow in the Local Early-Type Galaxy NGC 1266 // ApJ. VII 2011. 735, 2. 88. arXiv: 1104.2326.

Alatalo Katherine, Nyland Kristina, Graves Genevieve, Griffin Kristen Shapiro, Duc Pierre-Alain, Cappellari Michele, McDermid Richard M., Davis Timothy A., Crocker Alison F., Young Lisa M., Chang Philip, Scott Nicholas, Cales Sabrina L., Bayet Estelle, Blitz Leo, Bois Maxime, Bournaud Frédéric, Bureau Martin, Davies Roger L., Zeeuw P. Tim de, Emsellem Eric, Khochfar Sadegh, Krajnović Davor, Kuntschner

Harald, Morganti Raffaella, Naab Thorsten, Oosterloo Tom, Sarzi Marc, Serra Paolo, Weijmans Anne-Marie. NGC1266 as a Local Candidate for Rapid Cessation of Star Formation // ApJ. XII 2013. 780, 2. 186. arXiv: 1311.6469.

Allen D. A. An attempt to determine the circumstellar reddening law // Monthly Notices of the Royal Astronomical Society. II 1976. 174. 29P–33P.

Alonso-Herrero A., Pereira-Santaella M., García-Burillo S., Davies R. I., Combes F., Asmus D., Bunker A., Díaz-Santos T., Gandhi P., González-Martín O., Hernán-Caballero A., Hicks E., Hönig S., Labiano A., Levenson N. A., Packham C., Almeida C. Ramos, Ricci C., Rigopoulou D., Rosario D., Sani E., Ward M. J. Resolving the nuclear obscuring disk in the Compton-thick Seyfert galaxy NGC5643 with ALMA // ApJ. VI 2018. 859, 2. 144. arXiv: 1804.04842.

Audibert A., Combes F., García-Burillo S., Hunt L., Eckart A., Aalto S., Casasola V., Boone F., Krips M., Viti S., Muller S., Dasyra K., Werf P. van der, Martín S. ALMA captures feeding and feedback from the active galactic nucleus in NGC613 // arXiv e-prints. V 2019. arXiv:1905.01979.

Boquien M., Burgarella D., Roehlly Y., Buat V., Ciesla L., Corre D., Inoue A. K., Salas H. CIGALE: a python Code Investigating GALaxy Emission // A&A. II 2019. 622. A103. arXiv: 1811.03094.

Boquien Mederic, Buat Veronique, Perret Valentin. Impact of star formation history on the measurement of star formation rates // A&A. XI 2014. 571. A72. arXiv: 1409.5792.

Bouchet P., Lequeux J., Maurice E., Prevot L., Prevot-Burnichon M. L. The visible and infrared extinction law and the gas-to-dust ratio in the Small Magellanic Cloud // Astronomy and Astrophysics. VIII 1985. 149. 330–336.

Bruzual G., Charlot S. Stellar population synthesis at the resolution of 2003 // Monthly Notices RAS. X 2003. 344, 4. 1000–1028. arXiv: astro-ph/0309134.

Calzetti D., Armus L., Bohlin R. C., Kinney A. L., Koornneef J., Storchi-Bergmann T. The Dust Content and Opacity of Actively Star-Forming Galaxies // ApJ. IV 2000. 533, 2. 682–695. arXiv: astro-ph/9911459.

Calzetti D., Kennicutt R. C., Engelbracht C. W., Leitherer C., Draine B. T., Kewley L., Moustakas J., Sosey M., Dale D. A., Gordon K. D., Helou G. X., Hollenbach D. J.,

Armus L., Bendo G., Bot C., Buckalew B., Jarrett T., Li A., Meyer M., Murphy E. J., Prescott M., Regan M. W., Rieke G. H., Roussel H., Sheth K., Smith J. D. T., Thornley M. D., Walter F. The Calibration of Mid-Infrared Star Formation Rate Indicators // ApJ. IX 2007. 666, 2. 870–895. arXiv: 0705.3377.

Chabrier Gilles. Galactic Stellar and Substellar Initial Mass Function // PUBL ASTRON SOC PAC. VII 2003. 115, 809. 763–795. arXiv: astro-ph/0304382.

Charlot S., Fall S. Michael. A Simple Model for the Absorption of Starlight by Dust in Galaxies // ApJ. VIII 2000. 539, 2. 718–731. arXiv: astro-ph/0003128.

Cicone C., Maiolino R., Sturm E., Graciá-Carpio J., Feruglio C., Neri R., Aalto S., Davies R., Fiore F., Fischer J., García-Burillo S., González-Alfonso E., Hailey-Dunsheath S., Piconcelli E., Veilleux S. Massive molecular outflows and evidence for AGN feedback from CO observations // A&A. II 2014. 562. A21.

Combes F., Garcia-Burillo S., Casasola V., Hunt L. K., Krips M., Baker A. J., Boone F., Eckart A., Marquez I., Neri R., Schinnerer E., Tacconi L. J. ALMA observations of feeding and feedback in nearby Seyfert galaxies: an AGN-driven outflow in NGC 1433 // A&A. X 2013. 558. A124. arXiv: 1309.7486.

Conroy Charlie. Modeling the Panchromatic Spectral Energy Distributions of Galaxies // Annu. Rev. Astron. Astrophys. VIII 2013. 51, 1. 393–455. arXiv: 1301.7095.

Cresci G., Marconi A., Zibetti S., Risaliti G., Carniani S., Mannucci F., Gallazzi A., Maiolino R., Balmaverde B., Brusa M., Capetti A., Cicone C., Feruglio C., Bland-Hawthorn J., Nagao T., Oliva E., Salvato M., Sani E., Tozzi P., Urrutia T., Venturi G. The MAGNUM survey: Positive feedback in the nuclear region of NGC 5643 suggested by MUSE // A&A. X 2015. 582. A63. arXiv: 1508.04464.

Dale Daniel A., Helou George. The Infrared Spectral Energy Distribution of Normal Star-Forming Galaxies: Calibration at Far-Infrared and Submillimeter Wavelengths // ApJ. IX 2002. 576, 1. 159–168. arXiv: astro-ph/0205085.

Dale Daniel A., Helou George, Magdis Georgios E., Armus Lee, Díaz-Santos Tanio, Shi Yong. A Two-Parameter Model for the Infrared/Submillimeter/Radio Spectral Energy Distributions of Galaxies and AGN // ApJ. III 2014. 784, 1. 83. arXiv: 1402.1495.

Dasyra K. M., Combes F. Turbulent and fast motions of H2 gas in active galactic nuclei // A&A. IX 2011. 533. L10. arXiv: 1108.2888.

Dasyra K. M., Combes F., Oosterloo T., Oonk J. B. R., Morganti R., Salomé P., Vlahakis N. ALMA reveals optically thin, highly excited CO gas in the jet-driven winds of the galaxy IC 5063 // A&A. XI 2016. 595. L7.

Davis Timothy A., Krajnovic Davor, McDermid Richard M., Bureau Martin, Sarzi Marc, Nyland Kristina, Alatalo Katherine, Bayet Estelle, Blitz Leo, Bois Maxime, Bournaud Frederic, Cappellari Michele, Crocker Alison, Davies Roger L., Zeeuw P. T. de, Duc Pierre-Alain, Emsellem Eric, Khochfar Sadegh, Kuntschner Harald, Lablanche Pierre-Yves, Morganti Raffaella, Naab Thorsten, Oosterloo Tom, Scott Nicholas, Serra Paolo, Weijmans Anne-Marie, Young Lisa M. Gemini GMOS and WHT SAURON integral-field spectrograph observations of the AGN driven outflow in NGC 1266 // Monthly Notices of the Royal Astronomical Society. X 2012. 426, 2. 1574–1590. arXiv: 1207.5799.

Draine B. T., Li Aigen. Infrared Emission from Interstellar Dust. IV. The Silicate-Graphite-PAH Model in the Post-Spitzer Era // ApJ. III 2007. 657, 2. 810–837. arXiv: astro-ph/0608003.

Elmouttie E., Haynes R. F., Jones K. L., Ehle M., Beck R., Wielebinski R. The polarized radio lobes of the Circinus galaxy // Monthly Notices of the Royal Astronomical Society. VII 1995. 275, 1. L53–L59.

Faucher-Giguere C.-A., Quataert E. The physics of galactic winds driven by active galactic nuclei // Monthly Notices of the Royal Astronomical Society. IX 2012. 425, 1. 605–622. arXiv: 1204.2547.

A CO molecular gas wind 340 pc away from the Seyfert 2 nucleus in ESO 420-G13 probes an elusive radio jet. // . ???? 12.

Feruglio C., Fiore F., Carniani S., Piconcelli E., Zappacosta L., Bongiorno A., Cicone C., Maiolino R., Marconi A., Menci N., Puccetti S., Veilleux S. The multi-phase winds of Markarian 231: from the hot, nuclear, ultra-fast wind to the galaxy-scale, molecular outflow // A&A. XI 2015. 583. A99. arXiv: 1503.01481.

Feruglio Chiara, Maiolino Roberto, Piconcelli Enrico, Menci Nicola, Aussel Herve', Lamastra Alessandra, Fiore Fabrizio. Quasar feedback revealed by giant molecular outflows // A&A. VII 2010. 518. L155. arXiv: 1006.1655.

Fischer Jacqueline, Sturm Eckhard, González-Alfonso Eduardo, Graciá-Carpio Javier, Hailey-Dunsheath Steve, Poglitsch Albrecht, Contursi Alessandra, Lutz Dieter, Genzel Reinhard, Sternberg Amiel, Verma Aprajita, Tacconi Linda. Herschel PACS Spectroscopic Diagnostics of Local ULIRGs: Conditions and Kinematics in Mrk 231 // A&A. VII 2010. 518. L41. arXiv: 1005.2213.

Fitzpatrick Edward L. An average interstellar extinction curve for the Large Magellanic Cloud // The Astronomical Journal. XI 1986. 92. 1068–1073.

Fluetsch A., Maiolino R., Carniani S., Marconi A., Cicone C., Bourne M. A., Costa T., Fabian A. C., Ishibashi W., Venturi G. Cold Molecular Outflows in the Local Universe // Monthly Notices of the Royal Astronomical Society. XII 2018. arXiv: 1805.05352.

Fotopoulou C. M., Dasyra K. M., Combes F., Salomé P., Papachristou M. Complex molecular gas kinematics in the inner 5 kpc of 4C12.50 as seen by ALMA // arXiv:1908.01011 [astro-ph]. VIII 2019. arXiv: 1908.01011.

Fritz J., Franceschini A., Hatziminaoglou E. Revisiting the Infrared Spectra of Active Galactic Nuclei with a New Torus Emission Model // Monthly Notices of the Royal Astronomical Society. III 2006. 366, 3. 767–786. arXiv: astro-ph/0511428.

Garcia-Burillo S., Combes F., Usero A., Aalto S., Krips M., Viti S., Alonso-Herrero A., Hunt L. K., Schinnerer E., Baker A. J., Casasola F. Boone V., Colina L., Costagliola F., Eckart A., Fuente A., Henkel C., Labiano A., Martin S., Marquez I., Muller S., Planesas P., Almeida C. Ramos, Spaans M., Tacconi L. J., Werf P. P. van der. Molecular line emission in NGC1068 imaged with ALMA. I An AGN-driven outflow in the dense molecular gas // A&A. VII 2014. 567. A125. arXiv: 1405.7706.

García-González J., Alonso-Herrero A., Hönig S. F., Hernán-Caballero A., Almeida C. Ramos, Levenson N. A., Roche P. F., González-Martín O., Packham C., Kishimoto M. A mid-infrared statistical investigation of clumpy torus model predictions // Monthly Notices of the Royal Astronomical Society. IX 2017. 470, 3. 2578–2598. arXiv: 1706.07425.

George Richard, Ivison Rob, Smail Ian, Swinbank Mark, Hopwood Rosalind, Stanley Flora, Swinyard Bruce, Valtchanov Ivan, Werf Paul van der. Herschel reveals a molecular outflow in a z = 2.3 ULIRG // Monthly Notices of the Royal Astronomical Society. VIII 2014. 442, 2. 1877–1883. arXiv: 1402.6320.

González-Alfonso E., Fischer J., Spoon H. W. W., Stewart K. P., Ashby M. L. N., Veilleux S., Smith H. A., Sturm E., Farrah D., Falstad N., Meléndez M., Graciá-Carpio J., Janssen A. W., Lebouteiller V. Molecular outflows in local ULIRGs: energetics from multi-transition OH analysis // ApJ. II 2017. 836, 1. 11. arXiv: 1612.08181.

Goodman Jonathan, Weare Jonathan. Ensemble samplers with affine invariance // CAM-CoS. I 2010. 5, 1. 65–80.

Harnett J. I. Radio continuum observations of nearby galaxies // Monthly Notices of the Royal Astronomical Society. VIII 1987. 227, 4. 887–908.

Heckman Timothy M., Thompson Todd A. Galactic Winds and the Role Played by Massive Stars // arXiv:1701.09062 [astro-ph]. XI 2019. arXiv: 1701.09062.

Helou G., Soifer B. T., Rowan-Robinson M. Thermal infrared and nonthermal radio - Remarkable correlation in disks of galaxies // ApJ. XI 1985. 298. L7.

Hoenig S. F., Kishimoto M. The dusty heart of nearby active galaxies – II. From clumpy torus models to physical properties of dust around AGN // A&A. XI 2010. 523. A27. arXiv: 0909.4539.

Hogg David W., Bovy Jo, Lang Dustin. Data analysis recipes: Fitting a model to data // arXiv:1008.4686 [astro-ph, physics:physics]. VIII 2010. arXiv: 1008.4686.

Hopkins Philip F., Strauss Michael A., Hall Patrick B., Richards Gordon T., Cooper Ariana S., Schneider Donald P., Berk Daniel E. Vanden, Jester Sebastian, Brinkmann J., Szokoly Gyula P. Dust Reddening in SDSS Quasars // AJ. IX 2004. 128, 3. 1112–1123. arXiv: astro-ph/0406293.

Hubeny Ivan, Agol Eric, Blaes Omer, Krolik Julian. Non-LTE Models and Theoretical Spectra of Accretion Disks in Active Galactic Nuclei. III. Integrated Spectra for Hydrogen-Helium Disks // ApJ. IV 2000. 533, 2. 710–728. arXiv: astro-ph/9911317.

Husemann B., Wisotzki L., Sánchez S. F., Jahnke K. The properties of the extended warm ionised gas around low-redshift QSOs and the lack of extended high-velocity outflows // A&A. I 2013. 549. A43. arXiv: 1210.0566.

Ilbert O., McCracken H. J., Fevre O. Le, Capak P., Dunlop J., Karim A., Renzini M. A., Caputi K., Boissier S., Arnouts S., Aussel H., Comparat J., Guo Q., Hudelot P.,

Kartaltepe J., Kneib J. P., Krogager J. K., Floc'h E. Le, Lilly S., Mellier Y., Milvang-Jensen B., Moutard T., Onodera M., Richard J., Salvato M., Sanders D. B., Scoville N., Silverman J., Taniguchi Y., Tasca L., Thomas R., Toft S., Tresse L., Vergani D., Wolk M., Zirm A. Mass assembly in quiescent and star-forming galaxies since z=4 from UltraVISTA // A&A. VIII 2013. 556. A55. arXiv: 1301.3157.

Ivison R. J., Alexander David M., Biggs Andy D., Brandt W. N., Chapin Edward L., Coppin Kristen E. K., Devlin Mark J., Dickinson Mark, Dunlop James, Dye Simon, Eales Stephen A., Frayer David T., Halpern Mark, Hughes David H., Ibar Edo, Kovacs A., Marsden Gaelen, Moncelsi L., Netterfield Calvin B., Pascale Enzo, Patanchon Guillaume, Rafferty D. A., Rex Marie, Schinnerer Eva, Scott Douglas, Semisch C., Smail Ian, Swinbank A. M., Truch Matthew D. P., Tucker Gregory S., Viero Marco P., Walter Fabian, Weiss Axel, Wiebe Donald V., Xue Y. Q. BLAST: the far-infrared/radio correlation in distant galaxies // Monthly Notices of the Royal Astronomical Society. II 2010. 402, 1. 245–258. arXiv: 0910.1091.

Kennicutt Jr. Star Formation in Galaxies Along the Hubble Sequence // Annu. Rev. Astron. Astrophys. IX 1998. 36, 1. 189–231. arXiv: astro-ph/9807187.

Kneiske T. M., Mannheim K. Cosmic Star Formation Rate From Gamma-Ray Attenuation // arXiv:astro-ph/9912450. XII 1999. arXiv: astro-ph/9912450.

Krips M., Martin S., Eckart A., Neri R., Garcia-Burillo S., Matsushita S., Peck A., Stoklasova I., Petitpas G., Usero A., Combes F., Schinnerer E., Humphreys L., Baker A. J. SMA/PdBI multiple line observations of the nearby Seyfert2 galaxy NGC 1068: Shock related gas kinematics and heating in the central 100pc? // ApJ. VII 2011. 736, 1. 37. arXiv: 1105.6089.

Kroupa Pavel. On the variation of the Initial Mass Function // Monthly Notices of the Royal Astronomical Society. IV 2001. 322, 2. 231–246. arXiv: astro-ph/0009005.

Leitherer Claus, Schaerer Daniel, Goldader Jeffrey D., Delgado Rosa M. Gonzalez, Robert Carmelle, Kune Denis Foo, Mello Duilia F. de, Devost Daniel, Heckman Timothy M. Starburst99: Synthesis Models for Galaxies with Active Star Formation // ASTROPHYS J SUPPL S. VII 1999. 123, 1. 3–40. arXiv: astro-ph/9902334.

Leon S., Eckart A., Laine S., Kotilainen J. K., Schinnerer E., Lee S.-W., Krips M., Reunanen J., Scharwachter J. Nuclear starburst-driven evolution of the central region in NGC 6764 // arXiv:0707.1190 [astro-ph]. VII 2007. arXiv: 0707.1190.

Lodato G., Bertin G. The spectral energy distribution of self-gravitating protostellar disks // A&A. VIII 2001. 375, 2. 455–468. arXiv: astro-ph/0106325.

Lower Sidney, Narayanan Desika, Leja Joel, Johnson Benjamin D., Conroy Charlie, Davé Romeel. How Well Can We Measure the Stellar Mass of a Galaxy: The Impact of the Assumed Star Formation History Model in SED Fitting // arXiv:2006.03599 [astro-ph]. VI 2020. arXiv: 2006.03599.

Madau Piero, Dickinson Mark. Cosmic Star Formation History // Annu. Rev. Astron. Astrophys. VIII 2014. 52, 1. 415–486. arXiv: 1403.0007.

Maraston Claudia. Evolutionary population synthesis: models, analysis of the ingredients and application to high-z galaxies // Monthly Notices of the Royal Astronomical Society. IX 2005. 362, 3. 799–825. arXiv: astro-ph/0410207.

Mezcua M., Prieto M. A., Fernández-Ontiveros J. A., Tristram K., Neumayer N., Kotilainen J. K. The warm molecular gas and dust of Seyfert galaxies: two different phases of accretion? // arXiv:1506.07289 [astro-ph]. VI 2015. arXiv: 1506.07289.

Morganti Raffaella, Frieswijk Wilfred, Oonk Raymond J. B., Oosterloo Tom, Tadhunter Clive. Tracing the extreme interplay between radio jets and the ISM in IC5063 // A&A. IV 2013. 552. L4. arXiv: 1302.2236.

Morganti Raffaella, Oosterloo Tom, Oonk J. B. R., Frieswijk Wilfred, Tadhunter Clive. The fast molecular outflow in the Seyfert galaxy IC5063 as seen by ALMA // A&A. VIII 2015. 580. A1. arXiv: 1505.07190.

Murphy E. J., Condon J. J., Schinnerer E., Kennicutt Jr. R. C., Calzetti D., Armus L., Helou G., Turner J. L., Aniano G., Beirão P., Bolatto A. D., Brandl B. R., Croxall K. V., Dale D. A., Meyer J. L. Donovan, Draine B. T., Engelbracht C., Hunt L. K., Hao C.-N., Koda J., Roussel H., Skibba R., Smith J.-D. T. Calibrating Extinction-Free Star Formation Rate Diagnostics with 33GHz Free-Free Emission in NGC6946 // ApJ. VIII 2011. 737, 2. 67. arXiv: 1105.4877.

Netzer Hagai. Quasar discs. II - A composite model for the broad-line region // Monthly Notices of the Royal Astronomical Society. III 1987. 225. 55–72.

Netzer Hagai. Revisiting the Unified Model of Active Galactic Nuclei // Annu. Rev. Astron. Astrophys. VIII 2015. 53, 1. 365–408. arXiv: 1505.00811.

Onic D., Urosevic D., Arbutina B., Leahy D. On the existence of "radio thermally active" Galactic supernova remnants // ApJ. IX 2012. 756, 1. 61. arXiv: 1207.1778.

Pacifici Camilla, Charlot Stephane, Blaizot Jeremy, Brinchmann Jarle. Relative merits of different types of rest-frame optical observations to constrain galaxy physical parameters // Monthly Notices of the Royal Astronomical Society. IV 2012. 421, 3. 2002–2024. arXiv: 1201.0780.

Padmanabhan T. Theoretical Astrophysics : Galaxies And Cosmology, Vol 3. 2017.

Pandey A. K., Upadhyay K., Nakada Y., Ogura K. Interstellar extinction in the open clusters towards galactic longitude around 130 degrees // A&A. I 2003. 397, 1. 191–200. arXiv: astro-ph/0210680.

Pereira-Santaella M., Colina L., Garcia-Burillo S., Combes F., Emonts B., Aalto S., Alonso-Herrero A., Arribas S., Henkel C., Labiano A., Muller S., Lopez J. Piqueras, Rigopoulou D., Werf P. van der. Spatially resolved cold molecular outflows in ULIRGs // A&A. VIII 2018. 616. A171. arXiv: 1805.03667.

Peterson Bradley M. Reverberation mapping of active galactic nuclei // Publications of the Astronomical Society of the Pacific. III 1993. 105. 247–268.

Prevot M. L., Lequeux J., Maurice E., Prevot L., Rocca-Volmerange B. The typical interstellar extinction in the Small Magellanic Cloud // Astronomy and Astrophysics. III 1984. 132. 389–392.

Punsly Brian. An Independent Derivation of the Oxford Jet Kinetic Luminosity Formula // ApJ. IV 2005. 623, 1. L9–L12. arXiv: astro-ph/0503267.

Querejeta M., Schinnerer E., García-Burillo S., Bigiel F., Blanc G. A., Colombo D., Hughes A., Kreckel K., Leroy A. K., Meidt S. E., Meier D. S., Pety J., Sliwa K. AGN feedback in the nucleus of M51 // arXiv:1607.00010 [astro-ph]. VI 2016. arXiv: 1607.00010.

Rangwala Naseem, Maloney Philip R., Glenn Jason, Wilson Christine D., Rykala Adam, Isaak Kate, Baes Maarten, Bendo George J., Boselli Alessandro, Bradford Charles M., Clements D. L., Cooray Asantha, Fulton Trevor, Imhof Peter, Kamenetzky Julia, Madden Suzanne C., Mentuch Erin, Sacchi Nicola, Sauvage Marc, Schirm Maximilien R. P., Smith M. W. L., Spinoglio Luigi, Wolfire Mark. Observations of Arp 220 using Herschel-SPIRE: An Unprecedented View of the Molecular Gas in an Extreme Star Formation Environment // ApJ. XII 2011. 743, 1. 94. arXiv: 1106.5054.

Reid I. N., Kirkpatrick J. D., Liebert J., Burrows A., Gizis J. E., Burgasser A., Dahn C. C., Monet D., Cutri R., Beichman C. A., Skrutskie M. L Dwarfs and the Substellar Mass Function // ApJ. VIII 1999. 521, 2. 613–629. arXiv: astro-ph/9905170.

Richards Gordon T., Lacy Mark, Storrie-Lombardi Lisa J., Hall Patrick B., Gallagher S. C., Hines Dean C., Fan Xiaohui, Papovich Casey, Berk Daniel E. Vanden, Trammell George B., Schneider Donald P., Vestergaard Marianne, York Donald G., Jester Sebastian, Anderson Scott F., Budavari Tamas, Szalay Alexander S. Spectral Energy Distributions and Multiwavelength Selection of Type 1 Quasars // ASTROPHYS J SUPPL S. X 2006. 166, 2. 470–497. arXiv: astro-ph/0601558.

Rivera Gabriela Calistro, Lusso Elisabeta, Hennawi Joseph F., Hogg David W. AGNfitter: A Bayesian MCMC approach to fitting spectral energy distributions of AGN // ApJ. XII 2016. 833, 1. 98. arXiv: 1606.05648.

Rodríguez-Ardila A., Prieto M. A., Mazzalay X., Fernández-Ontiveros J. A., Luque R., Müller-Sánchez F. Powerful outflows in the central parsecs of the low-luminosity Active Galactic Nucleus NGC 1386 // Monthly Notices of the Royal Astronomical Society. IX 2017. 470, 3. 2845–2860. arXiv: 1706.01370.

Runnoe Jessie, Gültekin Kayhan, Rupke David. Does the Compact Radio Jet in PG 1700+518 Drive a Molecular Outflow? // ApJ. XII 2017. 852, 1. 8. arXiv: 1710.09450.

Rybicki George B., Lightman Alan P. Radiative processes in astrophysics. Weinheim: Wiley, 2004. (Physics textbook). OCLC: 255501661.

Sakamoto Kazushi, Aalto Susanne, Combes Francoise, Evans Aaron, Peck Alison. A Luminous Infrared Merger with Two Bipolar Molecular Outflows: ALMA and SMA Observations of NGC 3256 // ApJ. XII 2014. 797, 2. 90. arXiv: 1403.7117.

Sakamoto Kazushi, Aalto Susanne, Wilner David J., Black John H., Conway John E., Costagliola Francesco, Peck Alison B., Spaans Marco, Wang Junzhi, Wiedner Martina C. P-Cygni Profiles of Molecular Lines toward Arp 220 Nuclei // ApJ. VIII 2009. 700, 2. L104–L108. arXiv: 0906.5197.

Sakamoto Kazushi, Ho Paul T. P., Peck Alison B. Imaging Molecular Gas in the Luminous Merger NGC 3256 : Detection of High-Velocity Gas and Twin Gas Peaks in the Double Nucleus // ApJ. VI 2006. 644, 2. 862–878. arXiv: astro-ph/0603079.

Salim Samir, Narayanan Desika. The Dust Attenuation Law in Galaxies // arXiv:2001.03181 [astro-ph]. I 2020. arXiv: 2001.03181.

Salpeter Edwin E. The Luminosity Function and Stellar Evolution. // ApJ. I 1955. 121. 161.

Sandage A. Star formation rates, galaxy morphology, and the Hubble sequence // Astronomy and Astrophysics. VI 1986. 161. 89–101.

Sanders D. B., Scoville N. Z., Soifer B. T. Molecular gas in luminous infrared galaxies // The Astrophysical Journal. III 1991. 370. 158–171.

Schulz J., U. Fritze - v. Alvensleben , Möller C. S., Fricke K. J. Spectral and photometric evolution of simple stellar populations at various metallicities // A&A. IX 2002. 392, 1. 1–11.

Seaton M. J. Interstellar extinction in the UV // Monthly Notices of the Royal Astronomical Society. VI 1979. 187. 73P–76P.

Sharma Sanjib. Markov Chain Monte Carlo Methods for Bayesian Data Analysis in Astronomy // Annu. Rev. Astron. Astrophys. VIII 2017. 55, 1. 213–259. arXiv: 1706.01629.

Slone Oren, Netzer Hagai. The Effects of Disc Winds on the Spectrum and Black Hole Growth Rate of Active Galactic Nuclei // Monthly Notices of the Royal Astronomical Society. X 2012. 426, 1. 656–664. arXiv: 1207.7074.

Spoon H. W. W., Farrah D., Lebouteiller V., Gonzalez-Alfonso E., Bernard-Salas J., Urrutia T., Rigopoulou D., Westmoquette M. S., Smith H. A., Afonso J., Pearson C.,

Cormier D., Efstathiou A., Borys C., Verma A., Etxaluze M., Clements D. L. Diagnostics of AGN-driven Molecular Outflows in ULIRGs from Herschel-PACS Observations of OH at 119um // ApJ. IX 2013. 775, 2. 127. arXiv: 1307.6224.

Stone M., Veilleux S., Melendez M., Sturm E., Gracia-Carpio J., Gonzalez-Alfonso E. Search for Molecular Outflows in Local Volume AGN with Herschel-PACS // ApJ. VII 2016. 826, 2. 111. arXiv: 1605.06512.

Taylor G. B., Silver C. S., Ulvestad J. S., Carilli C. L. The Starburst in the Central Kiloparsec of Markarian 231 // ApJ. VII 1999. 519, 1. 185–190. arXiv: astro-ph/9902082.

Tombesi F., Melendez M., Veilleux S., Reeves J. N., Gonzalez-Alfonso E., Reynolds C. S. Wind from the black-hole accretion disk driving a molecular outflow in an active galaxy // Nature. III 2015. 519, 7544. 436–438. arXiv: 1501.07664.

Tsai An-Li, Matsushita Satoki, Kong Albert K. H., Matsumoto Hironori, Kohno Kotaro. First Detection of A Sub-kpc Scale Molecular Outflow in the Starburst Galaxy NGC 3628 // ApJ. VI 2012. 752, 1. 38. arXiv: 1204.3414.

Urošević Dejan, Pannuti Thomas G. Thermal emission at radio frequencies from supernova remnants and a modified theoretical –D relation // Astroparticle Physics. VII 2005. 23, 6. 577–587.

Vacca William D., Torres-Dodgen Ana V. Color excesses, intrinsic colors, and absolute magnitudes of Galactic and Large Magellanic Cloud Wolf-Rayet stars // ApJS. VIII 1990. 73. 685.

Vazdekis A., Sánchez-Blázquez P., Falcón-Barroso J., Cenarro A. J., Beasley M. A., Cardiel N., Gorgas J., Peletier R. F. Evolutionary Stellar Population Synthesis with MILES. Part I: The Base Models and a New Line Index System // Monthly Notices of the Royal Astronomical Society. III 2010. arXiv: 1004.4439.

Veilleux S., Melendez M., Sturm E., Gracia-Carpio J., Fischer J., Gonzalez-Alfonso E., Contursi A., Lutz D., Poglitsch A., Davies R., Genzel R., Tacconi L., Jong J. A. de, Sternberg A., Netzer H., Hailey-Dunsheath S., Verma A., Rupke D. S. N., Maiolino R., Teng S. H., Polisensky E. Fast Molecular Outflows in Luminous Galaxy Mergers: Evidence for Quasar Feedback from Herschel // ApJ. IX 2013. 776, 1. 27. arXiv: 1308.3139.

Wagner A. Y., Bicknell G. V. RELATIVISTIC JET FEEDBACK IN EVOLVING GALAXIES // ApJ. II 2011. 728, 1. 29.

Weaver R., McCray R., Castor J., Shapiro P., Moore R. Interstellar bubbles. II - Structure and evolution // ApJ. XII 1977. 218. 377.

Westfold K. C. The Polarization of Synchrotron Radiation. // ApJ. VII 1959. 130. 241.

Willott Chris J., Rawlings Steve, Blundell Katherine M., Lacy Mark. The emission line - radio correlation for radio sources using the 7C Redshift Survey // Monthly Notices of the Royal Astronomical Society. XI 1999. 309, 4. 1017–1033. arXiv: astro-ph/9905388.

Zschaechner Laura K., Walter Fabian, Bolatto Alberto, Farina Emanuele P., Kruijssen J. M. Diederik, Leroy Adam, Meier David S., Ott Jürgen, Veilleux Sylvain. The Molecular Wind in the Nearest Seyfert Galaxy Circinus Revealed by ALMA // ApJ. XI 2016. 832, 2. 142. arXiv: 1609.06316.